frontiers | Frontiers in Chemistry

ORIGINAL RESEARCH
published: 09 May 2022
doi: 10.3389/fchem.2022.880051

Al_2O_3-MgO Supported Ni, Mo, and NiMo Mixed Phosphidic-Sulphidic Phase for Hydrotreating of Stearic and Oleic Acids Into Green Diesel

Esneyder Puello-Polo[1]*, *Dana Arias*[1] and *Edgar Márquez*[2]

[1]Grupo de Investigación en Oxi/Hidrotratamiento Catalítico y Nuevos Materiales, Programa de Química-Ciencias Básicas Universidad del Atlántico, Barranquilla, Colombia, [2]Grupo de Investigación en Química y Biología, Departamento de Química y Biología, Universidad del Norte, Barranquilla, Colombia

The effect of the sulfur and metal-type content of MoP-S/γ-Al_2O_3-MgO, NiMoP-S/γ-Al_2O_3-MgO, and NiP-S/γ-Al_2O_3-MgO phosphide on hydroprocessing (HDO, HDCx-HDCn, HCK, HYD, and HYG) of fatty acids was studied. The catalysts were characterized by XRF, XRD, textural properties, XPS, Raman, Py-TPD, and EDS elemental mapping. The chemical analyses by X-ray fluorescence (XRF), EDS elemental mapping, and CHNS-O elemental analysis showed stoichiometric values Al/Mg = 38–40, Mo:Ni:P ~ 1, and S ≤ 4.5 wt % (this value means that the molar ratio Mo:S ~ 1.0:1.6, i.e., MoS_2); also EDS elemental mapping confirmed the presence of Mo, Ni, Al, O, P, Mg, and S with good distribution on Al_2O_3-MgO. The impregnation of metals leads to a decrease in the surface area and pore volume as follows NiMoP-S/γ-Al_2O_3-MgO < MoP-S/γ-Al_2O_3-MgO < NiP-S/γ-Al_2O_3-MgO < Al_2O_3-MgO < Al_2O_3 (unimodal pore size distribution), propitiating a pseudo bimodal pore size distribution with Dp-BJH between ~5–7 nm and 11.8–14.2 nm for the presence of MgO. XRD confirmed differences between metallic phosphates and phosphides, and XPS confirmed the presence at the surface of $Mo^{\delta+}(0 < \delta+ < 2)$, Mo^{4+}, Mo^{6+}, $Ni^{\delta+}(0 < \delta+ < 2)$, Ni^{2+}, S^{2-}, SO_4^{2-}, $P^{\delta+}$, and P^{5+} species. Raman revealed the presence of MoS_2 only in MoP-S/γ-Al_2O_3-MgO and NiMoP-S/γ-Al_2O_3-MgO, while the NiMoP-S/γ-Al_2O_3-MgO catalyst had a more significant number of Brønsted and Lewis sites, although the increasing temperature decreased the Lewis sites. MoP-S/γ-Al_2O_3-MgO was more active at HDO showing the highest production rate for octadecane of 53 mol/(g_{cat}·h), whereas NiP-S/γ-Al_2O_3-MgO was more active at HDCx-HDCn [45 mol/(g_{cat}·h)] and HCK [6 mol/(g_{cat}·h)]; meanwhile, NiMoP-S/γ-Al_2O_3-MgO had a mix of HDO [47 mol/(g_{cat}·h)] and HDCx-HDCn [41 mol/(g_{cat}·h)]. This showed production towards octadecane, heptadecane, and light hydrocarbons, meaning that the fatty acids were deoxygenated through bifunctional sites for hydrogenation (HYD) and hydrogenolysis (HYG) as follows: MoP-S/γ-Al_2O_3-MgO (K_1 = 0.08 and K_2 = 0.03 L/mol) < NiMoP-S/γ-Al_2O_3-MgO (K_1 = 0.25 and K_2 = 0.45 L/mol) < NiP-S/γ-Al_2O_3-MgO (K_1 = 2.5 and K_2 = 6.5 L/mol). For this reason, we considered that phosphide acts as a structural promoter with sulfur on its surface as a "mixed phosphidic-sulphidic species", allowing the largest generation of heptadecane and octadecane by the presence of BRIM sites for HYD and CUS sites for HYG.

Keywords: hydrotreating, Ni-Mo phosphidic-sulphidic, fatty acids, bifunctional sites, pseudo-first-order rate constants, adsorption constants

OPEN ACCESS

Edited by:
Jesus Gandara-Loe, KU Leuven, Belgium

Reviewed by:
Juan J. Villora-Pico, University of Alicante, Spain
Ping Liu, Changzhou University, China

***Correspondence:**
Esneyder Puello-Polo
esneyderpuello@mail.uniatlantico.edu.co

Specialty section:
This article was submitted to Catalytic Reactions and Chemistry, a section of the journal Frontiers in Chemistry

Received: *20 February 2022*
Accepted: *29 March 2022*
Published: *09 May 2022*

Citation:
Puello-Polo E, Arias D and Márquez E (2022) Al_2O_3-MgO Supported Ni, Mo, and NiMo Mixed Phosphidic-Sulphidic Phase for Hydrotreating of Stearic and Oleic Acids Into Green Diesel. Front. Chem. 10:880051. doi: 10.3389/fchem.2022.880051

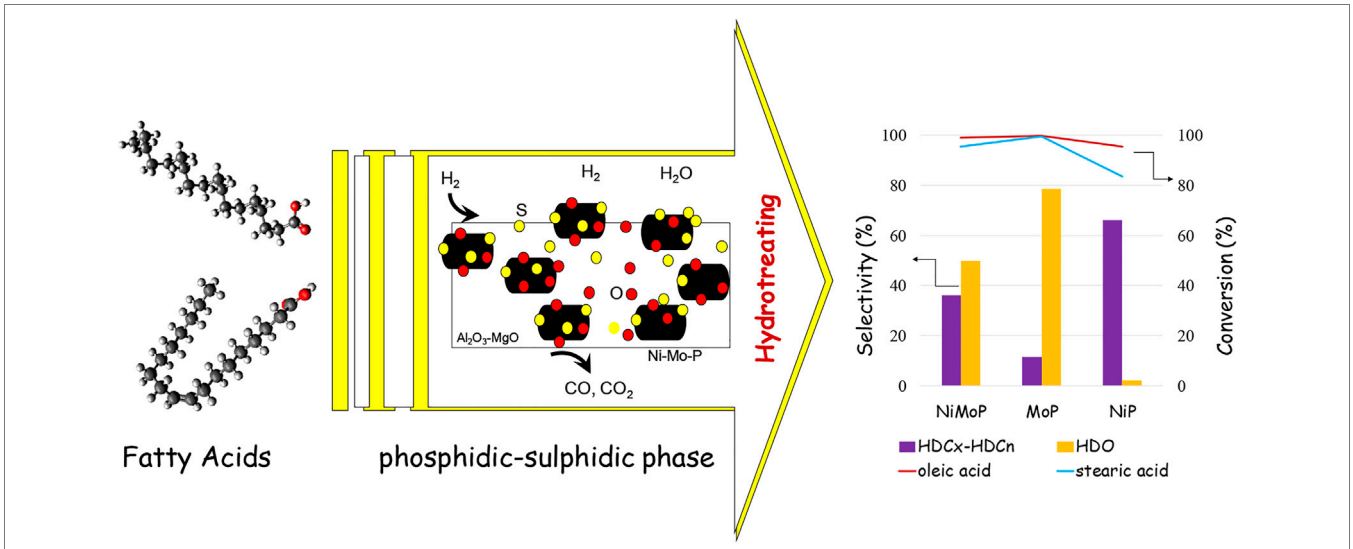

GRAPHICAL ABSTRACT | The sulfur and metal-type content in MoP-S/γ-Al_2O_3-MgO, NiMoP-S/γ-Al_2O_3-MgO, and NiP-S/γ-Al_2O_3-MgO influence the reaction pathways for hydrotreating fatty acids, improving the dispersion of MoS_2 on phosphide "mixed phosphidic-sulphidic species" and increasing the number of Lewis and Brönsted sites, which correlates well with the HDO and HDCx-HDCn pathways.

HIGHLIGHTS

- The phosphide acts as a structural promoter with sulfur on its surface, improving the catalytic activity.
- The Ni-Mo-P-S catalysts upgrade fatty acids through HDO using two bifunctional sites (hydrogenation and hydrogenolysis).
- Catalysts presented an Ni-Mo mixed phosphidic-sulphidic phase that could be the active phase in HDO on presulfiding phosphide catalysts.
- Bifunctional catalysts promote selection of fatty acid HYD by HDO and HDCx-HDCn pathways.
- Kinetics allowed describe the mechanism of oleic and stearic acids HYD by a Ni-Mo mixed phosphidic-sulphidic phase.

INTRODUCTION

Fossil fuels are the primary source of energy worldwide; however, the high demand to ensure the global economic and social development model has increasingly limited their availability. Thus, the increased consumption of oil derivatives quickly reduces world crude oil reserves (Gousi et al., 2017). Hence, there is concern about conserving non-renewable natural resources and evaluating alternative energies that gradually replace natural gas, coal, and fossil fuels in generation and not in the transport sector (Pearlson et al., 2013; Patil and Vaidya, 2018). Therefore, it seems essential to have more technically and economically viable possibilities to replace petroleum-derived fuels in the short and medium term. In this respect, biodiesel (FAME) is an alternative. However, FAME presents a series of disadvantages such as high oxygen content (35–40% w/w), high cloud point temperature, and poor oxidation stability which restrict its further development, corrosion in the equipment caused by the acid–base and salt-containing wastewater, a large number of neutralizing and purification steps in its manufacture, high viscosity which influences the increase of NOx emissions, and that the used catalyst cannot be recycled, which increases the capital and operating costs (Souza Macedo et al., 2019; Bezergianni and Dimitriadis, 2013).

A fact that has been gaining attention in recent years is the use of biofuels that have compositions resembling that of fossil-derived fuel and that avoid the presence of glycerol (petro-diesel), which is called "renewable diesel" (Donnis et al., 2009; Wang et al., 2018). This renewable diesel is composed mainly of an n-paraffin long chain that could ultimately replace petroleum-derived diesel fuel because both share identical composition and energy densities that are obtained from renewable sources (such as vegetable oils or animal fats) using catalytic hydrotreatment (HDT), and can be co-processed together with the heavy crude oil of equivalent molecular weights in conventional oil refineries (Yusuf et al., 2011; Helwani et al., 2009).

In general, the hydrotreating of triglycerides and fatty acids is the removal of oxygen yielding high-quality diesel fuel by three reaction pathways: decarboxylation (DCx), decarbonylation (DCn), and hydrodeoxygenation (HDO) (Gosselink et al., 2013; Susanto et al., 2016). Three central catalyst systems have been applied to the hydrotreatment/deoxygenation of triglycerides and fatty acids as follows: 1) Ni(Co)-Mo sulfides; 2) noble metals, mainly including Pt or Pd-based catalysts; and 3) non-noble transition metals (e.g.,

Ni, Mo, and others) (Immer et al., 2010; Sotelo-Boyás et al., 2011; Duan, 2017). However, sulfide catalysts are easily deactivated by oxidation (decreasing activity and contamination of products due to sulfur leaching), and noble metals are expensive; hence, these deficiencies restrict their practical use. On the other hand, non-noble transition metal catalysts have high catalytic activity and low cost, they are applicable in the deoxygenation process (Arend et al., 2011; Cecilia et al., 2013; Kandel et al., 2014; Smirnov et al., 2016), although they are poisoned by the nitrogenous compounds present in the fatty acids used for increased stability (Kamal-Eldin and Yanishlieva, 2002). In this regard, the transition metals: carbides, nitrides, borides, and phosphides-based solids have been identified as potential catalysts due to their attractive hydrogen transfer properties similar to those of noble metals. At the same time, they are sulfur, nitrogen, and oxygen-tolerant and have high thermal stability (leaching resistance), which is due to their particular structure resulting from the ligand and ensemble effects of carbon, nitrogen, boron, and phosphorus (Wang et al., 2011; Bui et al., 2012; Han et al., 2012).

The nature of the support can influence the product distribution of the HDO reaction (Kubička and Kaluža, 2010). The most widely used hydrotreating (HDT) support is alumina, which has strong interactions with compounds containing two oxygen atoms, showing deactivation due to coke formation (Centeno et al., 1995). In particular, Centeno et al. (1995) demonstrated that an essential cause for catalyst deactivation using alumina as the support in HDO of guaiacol, catechol, phenol, 4-methyl acetophenone, and p-cresol was due to coke formation. Hence, optimal acidity formulations have been proposed because they confer high catalyst hydrocracking (HCK) activity with a low coke deposition rate (Leyva et al., 2007). Notably, the addition of some oxides containing basic sites to the conventional support of hydrotreating catalysts, such as magnesium oxide (MgO) (Solis et al., 2004; Klicpera and Zdražil, 2002), decreases the metal-support interaction that promotes high dispersion on the catalyst support, cracking with low olefins hydrogenation, and the basic character of the support could inhibit coke formation (Klicpera and Zdražil, 2002). However, pure MgO is less convenient for co-hydrotreating of oxygen-containing feed because water and COx are formed during HDO which causes textural instability due to the presence of water that can destroy part of the surface of MgO (Kaluža et al., 2019). However, Yang et al., using CoMo(P)/MgO in HDO of bio-crude, highlighted that MgO-supported catalysts increased yields of reduced hydrocarbon products, such as benzene and cyclohexyl-aromatics, that is, less hydrocracking (Yang et al., 2009).

In addition, phosphorus was found to show beneficial effects on the activity of the hydrotreating reaction due to decreased coke formation and formation of new Lewis and Bronsted acid sites on the catalyst surface (Ferdous et al., 2004). Recently, Zhang et al. (2016) tested the addition of phosphorus to sulfided CoMoP/Al_2O_3 for HDO of pyrolysis oil, reducing the oxygen content from 41.8 wt % to 3 wt .%, which suggests that phosphorus promotes the activation of hydrogen in the hydrotreatment process. Hence, transition metal phosphide catalysts have been studied extensively because they are economical and less susceptible to hydrogenolysis of the C-C bond (Berenguer et al., 2016; Gonçalves et al., 2017). However, for triglycerides, HDO and fatty acids require two catalytically active sites: 1) a hydrogenation metallic site and 2) acid site for hydrogenolysis, dehydration, and isomerization (Zhao et al., 2011; Yu et al., 2019). Regarding those, it has been shown that transition metal phosphides are bifunctional in nature by the metal and P-OH groups/unreduced Ni^{2+}, respectively (Infantes-Molina et al., 2015; Lee and Oyama, 2006).

There are many reports of transition metal phosphides (especially Ni_2P) because they have shown excellent HDO performance (Lee and Oyama, 2006; Wang et al., 2002), with relevant studies on the active phase in HDO; hence, Z. Zhang et al. considering the works of Sawhill et al. (2005) and Li et al. (2014) showed that the Ni_2P phase is very active in the HDS and dehydrogenation processes; thus they studied the effects of the P/Ni ratio and the Ni content of phosphides on the HDO of methyl laurate to hydrocarbons. The results showed that HDO was promoted by increasing the P/Ni ratio and the Ni content in Ni_3P, $Ni_{12}P_5$, and Ni_2P. Likewise, Ni_xP_y showed much lower activity for decarbonylation, C-C hydrogenation, and methanation (Zhang et al., 2016).

Yang et al. (2012) performed a comparison of Ni_2P/SBA-15 and Ni/SBA-15 on HDO of methyl oleate, where Ni_2P/SBA-15 produced a high content of long-chain hydrocarbons, while Ni/SBA-15, due to the cracking reaction, gave a wider distribution of hydrocarbons. Guan et al. (2016) demonstrated the excellent HDO activities of methyl palmitate using nickel phosphides supported on MCM-41. However, in this study, Ni-based catalysts generally suffered from a high level of coke formation resulting in severe catalytic deactivation (Khzouz et al., 2013). Therefore, another active site needed to be added. Thus, several studies have been carried out with metallic combinations in phosphide catalysts (Feitosa et al., 2016; Chen et al., 2014a).

Rensel et al. (2013) revealed that FeMoP catalysts were highly selective for the rupture of the C-O bond in HDO of aryl ethers and phenol. A. Cho investigated the HDO of 2-MTHF on NiFeP, in which a synergistic effect between Ni and Fe on selectivity was observed (Cho et al., 2012). Pan et al. (2015) suggested that the catalytic performance of NiMoP catalysts in the HDO of methyl laurate is due to the charge transfer of Ni to Mo in $NiMoP_2$ or the incorporation of Mo into the structure of Ni_2P. In addition, Chen et al. found that the increase in TOF correlated with the increase of Mo on silica-supported Ni-Mo phosphides (Chen et al., 2014a; Pan et al., 2015). Yun et al. (2017) synthesized a series of NiMo bimetallic phosphides supported on MCM-41, and the HDO of γ-valerolactone was tested. The activity was related with the proportion of Ni in the catalyst, in the following order: Ni_2P/MCM-41 > NiMo(3:1)P/MCM-41 > NiMo(1:1)P/MCM-41 ~ (Ni_2P + MoP)/MCM-41 > NiMo(1:3)P/MCM-41 > MoP/MCM-41, suggesting that the Ni was the main active site, while Mo determined the selectivity. Although sulfided MgO-supported catalysts have been the object of a limited number of research studies (Zdražil, 2003; Klicpera and Zdražil, 2000);

catalytic application of Al_2O_3-MgO supported phosphides to HDO is almost nil. Furthermore, many studies hold that transition metal phosphides are potential catalysts in hydrotreating, but the exact nature of the active sites in these systems is still a matter of debate, and it is believed to be a stable phosphosulfide surface at hydrotreating conditions (Nelson et al., 2006). Hence, the results previously shown provide an incentive to explore the comparison of a series of Al_2O_3-MgO-supported nickel–molybdenum phosphides modified with sulfur, in which their activity is tested in HDO of fatty acids and gives insight into the catalyst structure-performance relationship.

EXPERIMENTAL

Preparation of Alumina Modified With Magnesium

The Al_2O_3-MgO catalytic supports with an Al/Mg atomic ratio = 38 were prepared by modifying traditional sol-gel synthesis (Puello-Polo et al., 2021; Méndez et al., 2013). In a typical experiment, appropriate amounts of aluminum (III) isopropylate {$Al[OCH(CH_3)_2]_3$, 99.8%, Sigma- Aldrich} was dispersed in 50 ml of isopropanol [$(CH_3)_2CHOH$, 98%, Sigma-Aldrich] under magnetic stirring at about 343 K until a homogeneous solution was obtained.

An aqueous solution of magnesium nitrate hexahydrate [6.1 mmol of $Mg(NO_3)_2{\cdot}6H_2O$, 98%, Sigma-Aldrich] was added to the solution of $Al[OCH(CH_3)_2]_3/(CH_3)_2CHOH$ at 350 K for 4 h and then cooled to room temperature until the polymerized solution of $Mg(NO_3)_2{\cdot}6H_2O/Al[OCH(CH_3)_2]_3$ in alcoholic medium was obtained. The solution was then slowly added to a surfactants solution that was obtained by homogenizing 56.5 mmol of tetramethylammonium hydroxide (TMAOH, 25% in H_2O, Sigma-Aldrich) in 30 ml of deionized water followed by the addition of 18.1 mmol of hexadecyltrimethylammonium bromide (99%, Sigma-Aldrich) until complete dispersion.

Simultaneously, the pH was adjusted between 8 and 10 with ammonium hydroxide (NH_4OH, 28.0%–30.0% NH_3 basis, Sigma-Aldrich), and kept under magnetic agitation for 2 h. The resulting mixture was aged for 5 days without stirring, and the formed gel was washed with deionized water until neutral pH. The solid obtained was dried at 393 K for 18 h, then the sample was calcined in a tubular furnace and treated with air at a flow rate of 50 $cm^3\ min^{-1}$ at 823 K for 8 h. Finally, the collected solid sample was milled, and the particles of a 100–140 mesh were collected for use (denoted as Al_2O_3-MgO).

Preparation of Catalyst and Precursors Supported on Al_2O_3-MgO

In all the runs, 3.5 g of Al_2O_3-MgO (Al/Mg = 38; mesh 100–140) was impregnated in excess of the pore volume to provide a uniform coating surface (Puello-Polo et al., 2021). The supported precursor was prepared by dropwise adding an aqueous solution of nickel (II) nitrate hexahydrate [$Ni(NO_3)_2{\cdot}6H_2O$, Aldrich, 99%] and/or ammonium heptamolybdate [$(NH_4)_6Mo_7O_{24}{\cdot}4H_2O$, Aldrich, 99%] with ammonium dihydrogen phosphate [$(NH_4)H_2PO_4$, Aldrich, 99%] in stoichiometric amounts of Mo:Ni:P = 1:1:1 (20 wt.% Mo) to a flask containing the support, under stirring at 343 K. The impregnation step lasted until removal of the solvent by evaporation. Finally, the mass obtained was further dried at 373 K for 12 h and the sample was calcined at 823 K for 4 h. The precursors were transferred to a fixed-bed tubular stainless-steel reactor (30 cm long, 20 mm I.D.) with an axial thermowell containing a thermocouple centered in the catalyst bed deposited on a quartz fiber bed. A tubular electrical furnace controlled by a temperature programmer (Electro Salgado Ltd.) was used to heat the reactor. The amount of the sample was approximately 2 g/batch. Pure H_2 was passed through the sample at a total flow rate of 50 $cm^3\ min^{-1}$. The temperature was increased at a linear rate of 1°C min^{-1} to the final temperature (973 K), which was held for 1 h (Liu et al., 2017). The samples were quenched to room temperature and then passivated by a 1% air/N_2 mixture for 1 h.

Catalyst and Support Characterization

Elemental analysis for Mo, Ni, P, S, and Mg was determined by X-ray fluorescence using a MagixPro PW–2440 Philips instrument. The textural characteristics of the catalysts were determined employing the physisorption of N_2 at 77 K using a Micromeritics 3FLEX™ instrument. The Brunauer–Emmett–Teller multipoint method (BET) calculated the surface areas of samples, and total pore volume and pore size distribution were determined from the desorption branch of the isotherm using the Barret–Joyner–Halenda (BJH) model (Barrett et al., 1951). The total pore volume was estimated by summation of microporous and mesoporous volumes. The surface area due to micropores (S_{micro}) was obtained from a mass balance, i.e., $S_{micro} = S_{BET} - S_{ext}$ (Puello-Polo et al., 2018). XRD analysis of the samples was carried out using a SIEMENS D-5005 diffractometer with a Cu Kα radiation source (λ = 1.5418 Å) and Ni filter, within the range $5^\circ \leq 2\theta \leq 90^\circ$. For the identification of the crystallographic phase(s) (International Centre for Diffraction Data, 1995), the JCPDS data files were preferentially used for $(NH_4)_3PO_4(MoO_3)_{12}{\bullet}4H_2O$ (card no. 09-0408), MoP (card no. 24-0771), NiMoP (card no. 031-0873), and γ-Al_2O_3 (card no. 10-0425). Raman spectra of the phosphides were obtained in a Horiba Scientific Raman microspectrometer with LabRAM HR Evolution at room temperature using the 532 nm line and a between 41.1 and 56.1 μW He–Ne laser excitation source through an Olympus TM BX41 optical microscope. FTIR measured the pyridine adsorption on the different samples with the aim to monitor both the type (Brønsted or Lewis acidic sites) and their relative abundance (Crépeau et al., 2006). A thin wafer of the pure catalyst powder was made (8 mg cm^{-2}) and placed into a special IR cell; then, the sample was immediately pretreated under vacuum at 773 K for 4 h. Afterwards, the sample temperature was decreased to 423 K and exposed to pyridine vapor (1.5 m bar pressure) for 5 min. The physically adsorbed pyridine fraction was removed by degassing the sample for 30 min, and the IR spectra were collected. Spectra were recorded in 256 scans using a Nicolet FTIR spectrometer, and the data analysis was performed with the spectrometer software Omnic 8.1. The adsorbed pyridine

on Brönsted and Lewis acid sites was calculated under different desorption temperatures (50, 100, 200, and 300°C). The acidity due to Brönsted and Lewis sites (L and B, respectively), in μmol Py/g, was calculated as:

$$L = \frac{\pi/4\,(D^2)A_{1450}}{(IMEC_L)m_{solid}} \qquad B = \frac{\pi/4\,(D^2)A_{1540}}{(IMEC_B)m_{solid}}$$

Where D is the diameter of self-supported wafers, A1450 and A1540 are the integrated area below the bands at 1,450 and 1,540 cm^{-1} in the absorption spectrum of pyridine, IMECB and IMECL are the integrated molar extinction coefficients corresponding to the bands at 1,450 and 1,540 cm^{-1}, IMECL = 222 cm/μmol and IMECB = 167 cm/μmol (Emeis, 1993), and m_{solid} is the mass of the sample (g).

The sulfided phosphides' surface composition was determined through X-ray photoelectron spectroscopy (XPS) with a Thermo Scientific K-Alpha spectrometer, equipped with a dual (non-monochromatic) Mg/Al anode, operated at 400 W and under a vacuum better than 10^{-9} torr. Calibration of the instrument was carried out employing the Au $4f_{7/2}$ line at 83.9 eV. A dual flood gun source of low-energy electrons and Ar^+ ions was used during all measurements to prevent surface charging. The internal referencing of binding energies was made using the dominating Al 2p band of the support at 74.4 eV. After *in situ* sulfiding for XPS analysis, samples were immersed in purified n-hexane and quickly transferred to the XPS instrument, where the solvent was slowly removed under vacuum (Farojr and Dossantos, 2006). Curve fitting of the spectra was carried out using the XPSPEAK version 4.1 and XPS GRAPH programs, employing a standard nonlinear least-squares curve fitting routine and mixed Gaussian/Lorentzian peak shapes of variable proportion, after baseline subtraction by the Shirley method.

Scanning electron microscopy (SEM) with energy-dispersive X-ray spectroscopy (EDX) analysis were undertaken using a field emission scanning electron microscope (JEOL, model JSM-7800F, Japan) operated at 1 kV. The EDX chemical elemental mapping images and elemental analysis were acquired simultaneously at 15 kV using the energy-dispersive X-ray spectroscopy interconnected with the same JEOL 7800F instrument.

Sulfur elemental analysis of the mixed phosphidic-sulphidic phase was carried out using a combustion method using a Fisons EA 1108 CHNS-O analyzer.

Hydrotreatment Test of Fatty Acids

To remove the passivation layer and attain a stable and reproducible Ni-Mo mixed phosphidic-sulphidic phase (Puello-Polo and Brito, 2008), before the catalytic reaction, the phosphide and passivated forms were activated *in situ* under a 0.5 vol % CS_2/heptane mixture and H_2 (50 cm^3 min^{-1}) at 300°C for 1 h. The hydrotreatment of the mix of fatty acids (oleic and stearic acids) was conducted under conventional hydrotreating conditions in a 600 ml batch reactor (Trejo et al., 2005). In a typical reaction, 0.5 g of catalyst, 1.6 g of fatty acids (oleic acid: stearic acid = 1:1), and 78.4 g of n-dodecane were introduced into the batch reactor, and subsequently, the reactor was purged three times by N_2 at ambient temperature and then pressured to 3.1 MPa H_2. The reaction mixture was then heated from room temperature to reaction temperature (573 K) and target H_2 pressure (5 MPa H_2) for 6 h under constant stirring (300 rpm). The consumption during the reaction of fatty acids and the products contained in the liquid phase were collected and injected into a CG-2014 Shimadzu equipped with a flame ionization detector (FID). The products were identified and confirmed by GC-MS Agilent technology 7890B GC System-5977A MSD and compared to standards. The effluents sampling of the reactor occurred at 0, 90, 180, 270, and 360 min, and the catalytic activities of the catalysts were determined (Puello-Polo et al., 2021). The conversion of fatty acids was calculated as the proportion of fatty acids converted concerning the fatty acids feedstock at 6 h of reaction as defined in **Eq. 1**:

$$\%\,FA\,conversion = \frac{FA_0 - FA_t}{FA_0} \times 100 \tag{1}$$

where FAo and FAt are the fatty acid molar concentration (mol L^{-1}) at the beginning and at 6 h, respectively.

Additionally, the yield of fatty acids HYD was calculated as the proportion of a product formed in relation to the fatty acids consumed during the reaction as defined in **Eq. 2**:

$$\%\,\text{yield}\,i = \frac{C_i}{FA_0} \times 100 \tag{2}$$

where FAo and Ci are the fatty acid molar concentration (mol L^{-1}) at the beginning and product formed at 6 h, respectively.

Both the supporting alumina and the Mg-modified alumina showed negligible fatty acids conversion in the reaction. Established procedures verified the absence of mass and heat flow transport effects (Froment et al., 2011). All experiments reported in this work (synthesis protocols, characterizations, and catalytic activity measurements) were carried out at least in triplicate. Good reproducibility was verified, better than 10% in all quantitative measurements.

All the reactions were assumed irreversible due to the excess of hydrogen (considered constant), whereby the reactions were considered pseudo-first-order. The semi-empirical kinetic model of fatty acids HYD is the generalized Hinshelwood-Hougen-Watson model (Satterfield et al., 1980). It was calculated according to the results obtained by Kumar and Hachemi, suggesting a modified HYD reaction network as presented in **Scheme 1** (Hachemi and Murzin, 2018; Kumar et al., 2014), the reaction rate was defined in **Eq. 3**.

$$r_{ij} = \frac{k_{ij}C_i}{\left(1 + \sum_m K_m C_m\right)^Z} \tag{3}$$

Where rij (mol/L h) is the rate of conversion of compound i to compound j, C (mol/L) is the concentration, kij (L/mol h) is the apparent kinetic rate constant (including surface reaction and adsorption contributions), and Km (L/mol) is the

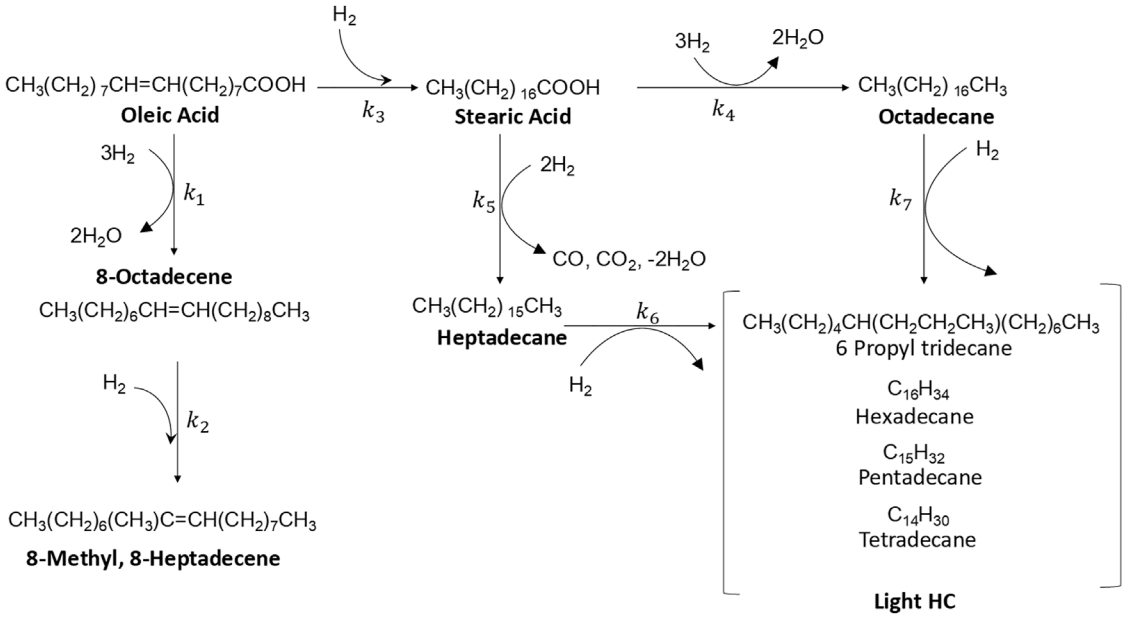

SCHEME 1 | Reaction pathways for hydrotreating oleic and stearic acids.

TABLE 1 | Experimental composition of the Al_2O_3-MgO supported NiMo mixed phosphidic-sulphidic phase.

Solid	Experimental composition (wt%)-XRF					Experimental composition (wt%)-EDS					CHONS elemental analysis
	Mo	Ni	P	S	$\frac{Al}{Mg}$	Mo	Ni	P	S	$\frac{Al}{Mg}$	% wt S
NiP-S/γ-Al_2O_3-MgO		11.6	6.9	2.2	40		8.1	5.5	1.0	41	2.0
MoP-S/γ-Al_2O_3-MgO	19.0		6.1	6.2	40	17.5		4.9	2.1	37	2.9
NiMoP-S/γ-Al_2O_3-MgO	20.1	10.5	6.2	5.1	38	21.5	8.5	7.1	3.3	41	4.5

wt %: percentage by weight; composition nominal: Ni:Mo:P = 1.0, Al/Mg = 38 (2 wt % MgO); γ-Al_2O_3-MgO experimental data: Al/Mg = 42 (3.5 wt % MgO).

adsorption parameter of individual compounds. Thus, Z represents the number of surface sites required for the reaction.

In **Scheme 1**, a variety of complex reactions can be seen during the one-step hydroprocessing of fatty acids, including isomerization, hydrodeoxygenation, hydrocracking, hydrodecarbonylation, and hydrodecarboxylation. This reveals that oleic acid (unsaturated acids) undergoes hydrosaturation to form stearic acid and isomerization to produce 8-octadecene and 8-methyl-8-heptadecene; subsequently, the saturated stearic acid is converted into long-chain hydrocarbons by dehydration, decarbonylation, and decarboxylation reactions to form heptadecane, octadecane, and light hydrocarbons (light HC, <C17) as identified by GC-MS, which accounted for more than 98% of the total products.

The system of differential equations to calculate the apparent rate and equilibrium adsorption constants was solved using the Mathematics-Wolfram software version 11.1. The nonlinear parameter estimations were calculated until converged by minimizing the deviation from theoretical and experimental concentrations (objective function) at different times using the Levenberg–Marquardt algorithm of GNU Octave version 4.2.2 through the Optim package, with the constraint of non-negativity. In this approach, the apparent rate and equilibrium adsorption constants of the oleic and stearic acids HYD were calculated as k_1, k_2, k_3, k_4, k_5, k_6, and k_7 and K_1 and K_2, respectively.

Finally, the fatty acids HYD activities of the catalysts were reported as pseudo-first-order rate constant for oleic and stearic acid disappearance normalized by the moles of oleic or stearic acids per weight (m_{cat}, g) of the catalyst after 6 h of reaction time. Therefore, the HDO, DCx-DCn, and hydrocracking (HCK) activities were reported after 6 h of reaction time as defined in **Eqs 4–6**:

$$\text{HDO activity} = k_1 + k_4 \quad (4)$$

$$\text{DCx} - \text{DCn activity} = k_5 \quad (5)$$

$$\text{HCK activity} = k_6 + k_7 \quad (6)$$

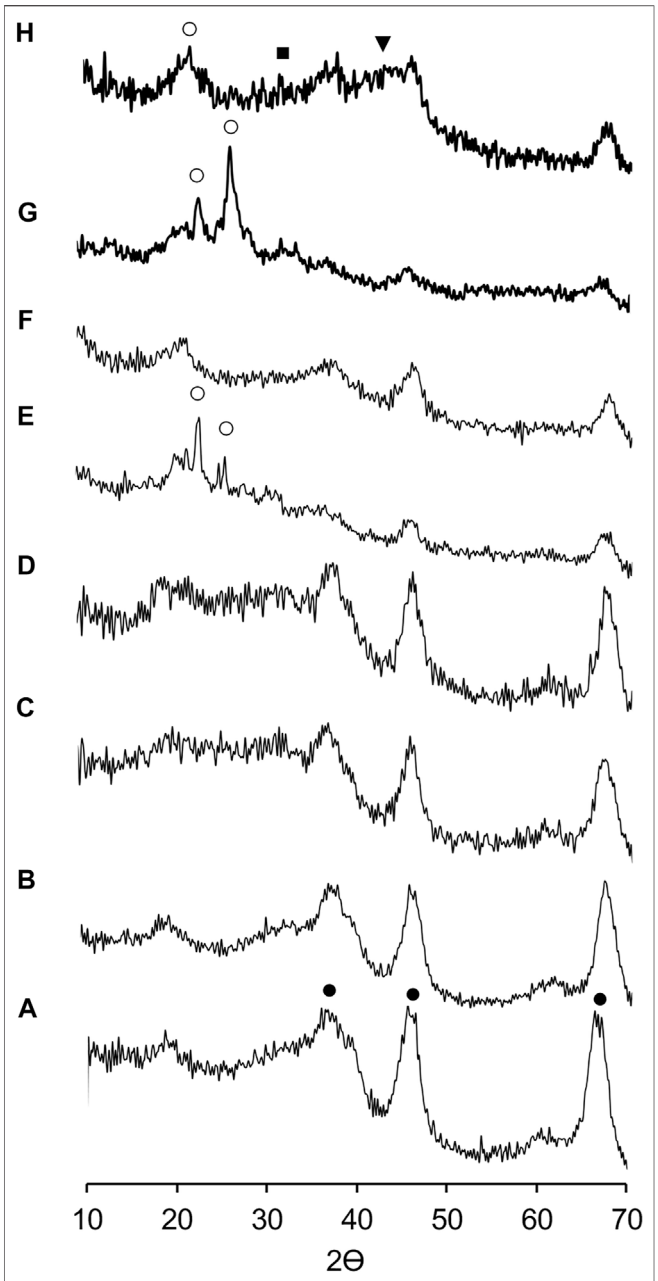

FIGURE 1 | X-ray diffraction patterns of supports and the Al_2O_3-MgO supported NiMo mixed phosphidic-sulphidic phase: **(A)** Al_2O_3, **(B)** Al_2O_3-MgO, **(C)** NiP-O/γ-Al_2O_3-MgO, **(D)** NiP-S/γ-Al_2O_3-MgO, **(E)** MoP-O/γ-Al_2O_3-MgO, **(F)** MoP-S/γ-Al_2O_3-MgO, **(G)** NiMoP-O/γ-Al_2O_3-MgO, and **(H)** NiMoP-S/γ-Al_2O_3-MgO. (●) γ-Al_2O_3, (■) MoP, (▼) NiMoP, and (○) $(NH_4)_3PO_4(MoO_3)_{12}{\bullet}4H_2O$.

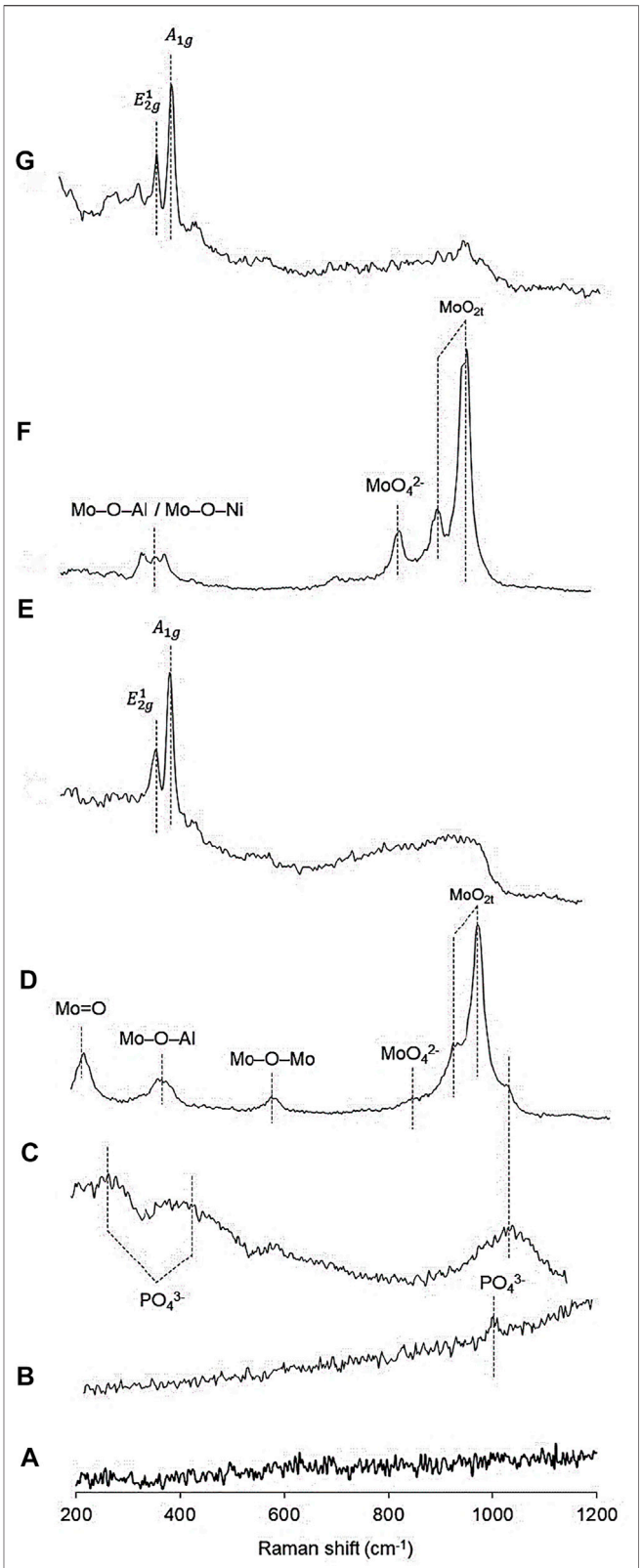

FIGURE 2 | Raman spectra of the Al_2O_3-MgO supported NiMo mixed phosphidic-sulphidic phase**: (A)** Al_2O_3-MgO, **(B)** NiP-O/γ-Al_2O_3-MgO, **(C)** NiP-S/γ-Al_2O_3-MgO, **(D)** MoP-O/γ-Al_2O_3-MgO, **(E)** MoP-S/γ-Al_2O_3-MgO, **(F)** NiMoP-O/γ-Al_2O_3-MgO, and **(G)** NiMoP-S/γ-Al_2O_3-MgO.

RESULTS AND DISCUSSION

Chemical Analysis

Results obtained from XRF and EDX chemical analyses of Al_2O_3-MgO, NiP-S/γ-Al_2O_3-MgO, MoP-S/γ-Al_2O_3-MgO, and NiMoP-S/γ-Al_2O_3-MgO are shown in **Table 1**. The differences between

experimental and nominal contents for all catalysts were within experimental accuracy, whose deviations could be related to the steps applied to synthesizing the supports and catalysts (Puello-Polo et al., 2020). Hence, the Al/Mg, Ni:Mo, Ni:P, and Mo:Ni:P atomic ratios proposed were similar to the designed formulation of the supports and catalysts in this work. On the other hand, sulfur elemental analysis of the mixed phosphidic-sulphidic phase showed low content of sulfur <4 wt %, suggesting that the phosphides were not degraded because the total generation of metallic sulfides with our catalysts resulted in 10–23 wt % of S (see CHONS chemical analyses); therefore, only changes in the surface were observed as will be shown in the XPS analysis (Nelson et al., 2006).

XRD Analysis

The **Figure 1** shows the XRD patterns of mixed phosphidic-sulphidic phase and their precursors (metallic phosphates). The XRD patterns revealed differences between metallic phosphates and mixed phosphidic-sulphidic phase except for the NiP-O/γ-Al_2O_3-MgO (C and D patterns), which does not show characteristic signs of a metal phosphate or phosphide. It is worth mentioning that it is difficult to distinguish the diffraction peaks, referring to phosphide/sulfide and MgO (~2 wt%) in all the catalysts, probably because alumina amorphism, crystallites size (too small to give XRD signals) or the particles of phosphidic-sulphidic composite well dispersed on the γ-Al_2O_3-MgO matrix. However, due to the changes in the difractograms between metallic phosphates and phosphides, it lets assume that under the reaction conditions it is likely to generate these types of species, such as MoP at 2θ = 32.17 and γ-Al_2O_3 at 2θ = 67.10, 45.90, 37.64 in MoP-S/γ-Al_2O_3-MgO (E and F patterns); and NiMoP at 2θ = 43.19; $(NH_4)_3PO_4(MoO_3)_{12}\bullet 4H_2O$ at 2θ = 26.47, 21.51 and γ-Al_2O_3 for NiMoP-S/γ-Al_2O_3-MgO as will be displayed in XPS (G and H patterns).

Raman

Figure 2 shows the Raman spectra of the precursors and catalysts which revealed the absence of bands corresponding to the γ-Al_2O_3-MgO support. The NiP-O/γ-Al_2O_3-MgO precursor presented the main band at approximately 1,000 cm^{-1}, characteristic of antisymmetric stretching modes of P-O bonds (PO_4^{3-} stretching) (Butt et al., 2004; Yang et al., 2019), while NiP-S/γ-Al_2O_3-MgO showed three peaks around 425, 300, and 1,126 cm^{-1} that were assigned to the PO_4^{3-} bending modes (Yang et al., 2019). MoP-O/γ-Al_2O_3-MgO showed bands at 1,018 (shoulder), 960, 922, 830 (shoulder), 588, 382, and 226 cm^{-1} (shoulder) that could be assigned to the PO_3^{4-} group, MoO_{2t} symmetric stretching, MoO_4^{2-}, Mo–O–Mo bridge stretching, stretching of Mo–O–Al entities, and terminal Mo=O of octahedral MoO_4^{2-} species, respectively (Wang et al., 2016; Botto et al., 1992). NiMoP-O/γ-Al_2O_3-MgO displayed bands at 1,000 (shoulder), 952, 906, 838, 360–390, and 224 cm^{-1} that could be assigned to the PO_3^{4-} group, MoO_{2t} symmetric stretching, MoO_4^{2-}, stretching of Mo–O–Al or Mo–O–Ni entities, and terminal Mo=O of octahedral MoO_4^{2-} species, respectively (Botto et al., 1992). The Raman spectra of the Mo and NiMo phosphides after passivation and sulfidation at 573 K are shown in **Figure 2**, which do not present Raman bands attributed to phosphates and oxidic phases (E and G). In this figure, MoP-S/γ-Al_2O_3-MgO and NiMoP-S/γ-Al_2O_3-MgO presented two typical Raman peaks at 380 and 405 cm^{-1} for the E^1_{2g} and A_{1g} active modes, characteristic of the bulk or multilayered MoS_2 (Li et al., 2012). We suppose that the phosphides phase was absent because of the processes of oxidation-sulfiding or the metal/P ratio (Yang et al., 2020). The bands' intensity and shape depended on the solid obtained; thus, the vibration bands' intensity corresponding to the mixed phosphidic-sulphidic phase was higher than phosphates due to hydrogenation treatment, which is likely to induce the growth of crystallites.

Textural Properties

All the N_2 physisorption isotherms of Al_2O_3, Al_2O_3-MgO, NiP-S/γ-Al_2O_3-MgO, MoP-S/γ-Al_2O_3-MgO, and NiMoP-S/γ-Al_2O_3-MgO were type IV in the IUPAC classification (**Figure 3**) (Thommes et al., 2015). The hysteresis loops showed that Al_2O_3, Al_2O_3-MgO, and NiP-S/γ-Al_2O_3-MgO were H1 due to uniform mesopores; while MoP-S/γ-Al_2O_3-MgO and NiMoP-S/γ-Al_2O_3-MgO were H2 related with ink-bottle and uniform mesopores. The isotherms behavior revealed the composite type's influence on textural properties of the catalysts. The surface area and pore volume of all solids were shown to increase as follows except for Al_2O_3 and Al_2O_3-MgO: NiMoP-S/γ-Al_2O_3-MgO < MoP-S/γ-Al_2O_3-MgO < NiP-S/γ-Al_2O_3-MgO < Al_2O_3-MgO < Al_2O_3. This behavior is related to the Ni, Mo, P, and Mg migration into the support pores, generating microporosity during the impregnation process, as shown in **Table 2** for the S_{micro}/S_{BET} ratio, although larger pores were of interest in this study due to the large size of the fatty acids.

The Al_2O_3-MgO support increased the pore volume and diameter, which means that the Mg^{2+} ions were incorporated into the Al_2O_3 structure [r Mg^{2+}(0.072 nm) > r Al^{3+} (0.051 nm)] due to the sol-gel method that forms Al-O-Mg bonding in the process of gelation (Puello-Polo et al., 2018; Ueno et al., 1983). In this respect, it is expected that when Mg is incorporated into the alumina structure it would improve the dispersion of Ni, Mo, and P on the support.

The pore diameters of the catalysts and supports were principally located in the mesoporous range (2–50 nm) (Thommes et al., 2015), with values of BJH mesopore mean size between 6.5 and 11.2 nm in the order: Al_2O_3 < NiMoP-S/γ-Al_2O_3-MgO < MoP-S/γ-Al_2O_3-MgO < NiP-S/γ-Al_2O_3-MgO < Al_2O_3-MgO. In addition, the Al_2O_3-MgO and phosphides isotherms showed a slight jump in their adsorption branch at high relative pressures, suggesting a certain bimodality in pore size distribution with pore sizes below ~7 and 11 nm, whereas Al_2O_3 displayed a unimodal pore size distribution (see **Table 2** and the box in **Figure 3**) (Uhlig et al., 2018).

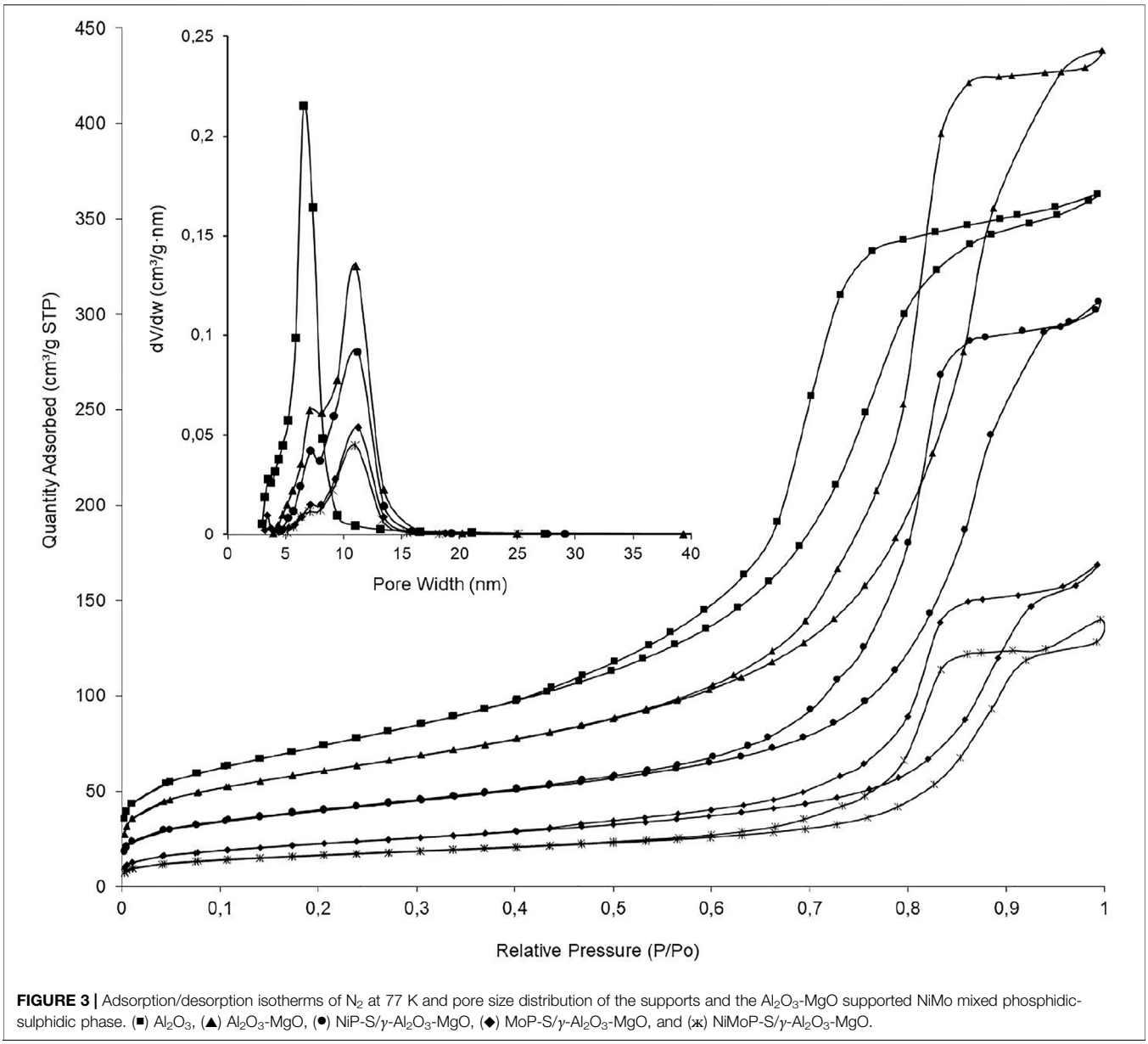

FIGURE 3 | Adsorption/desorption isotherms of N_2 at 77 K and pore size distribution of the supports and the Al_2O_3-MgO supported NiMo mixed phosphidic-sulphidic phase. (■) Al_2O_3, (▲) Al_2O_3-MgO, (●) NiP-S/γ-Al_2O_3-MgO, (◆) MoP-S/γ-Al_2O_3-MgO, and (ж) NiMoP-S/γ-Al_2O_3-MgO.

TABLE 2 | Textural properties of the Al_2O_3-MgO supported NiMo mixed phosphidic-sulphidic phase.

Solid	Specific surface area and porous characteristics							
	S_{BET} (m^2/g)	V_{meso} (cm^3/g)	V_{micro} (cm^3/g)	V_T (cm^3/g)	D_p (nm)	S_{EXT}	S_{micro}	S_{micro}/S_T
γ-Al_2O_3	265	0.566	0.0006	0.57	6.5	258	7	2.6
γ-Al_2O_3-MgO	213	0.659	0.008	0.67	8.1; 11.1	193	20	9.4
NiP-S/γ-Al_2O_3-MgO	141	0.471	0.005	0.48	7.3; 11.2	129	12	8.5
MoP-S/γ-Al_2O_3-MgO	80	0.258	0.0005	0.26	7.0; 11.2	77	3	3.8
NiMoP-S/γ-Al_2O_3-MgO	58	0.193	0.0014	0.19	7.0; 11.0	54	4	6.9

S_{BET}, BET surface area; S_{micro}, micropores surface area; S_{ext}, external surface area; S_{micro}/S_{BET}, fraction of the micropores area to the total surface area; V_T, total volume of pores; Dp, mean pore diameter; V_{meso}, mesopores volume; V_{micro}, micropores volume.

XPS Analysis

The XPS technique was applied to find out the composition and show that metal phosphides were formed in NiP-S/γ-Al_2O_3-MgO, MoP-S/γ-Al_2O_3-MgO, and NiMoP-S/γ-Al_2O_3-MgO. In the Ni 2p region spectra of NiP-S/γ-Al_2O_3-MgO, **Figure 4B** shows three Ni $2p_{3/2}$ peaks centered at 852.4,

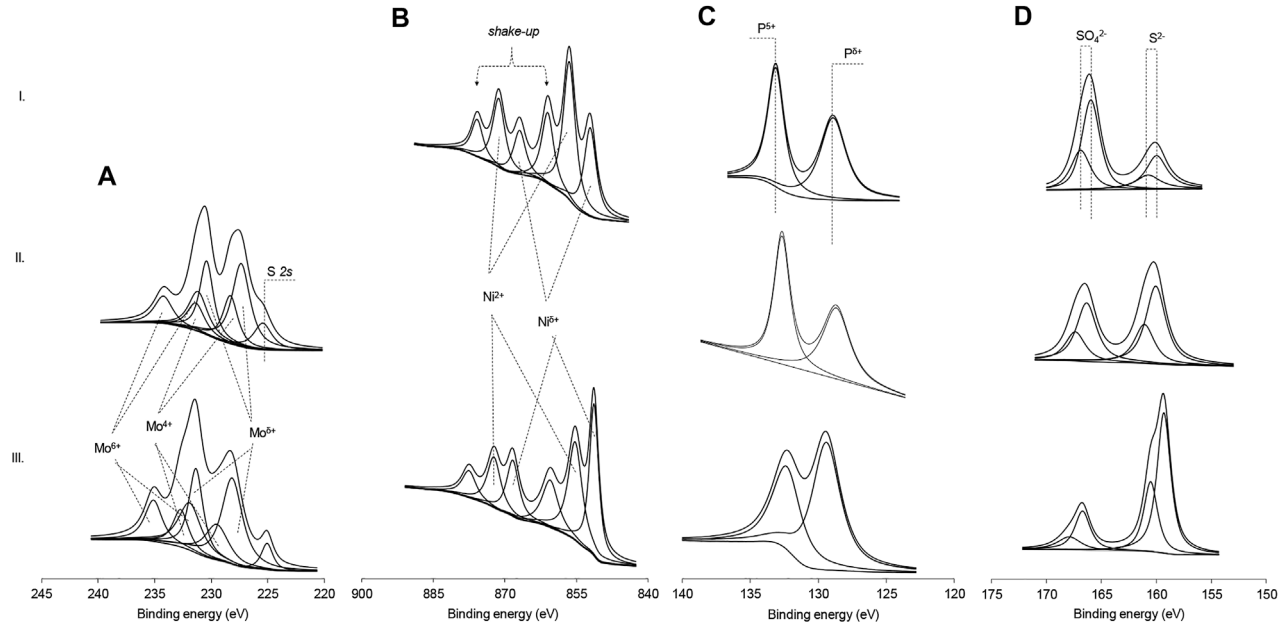

FIGURE 4 | X-ray photoelectron spectra of Mo 3d, Ni 2p, P 2p, and S 2p regions of the Al_2O_3-MgO-supported NiMo mixed phosphidic-sulphidic phase: **(A)** Mo 3d, **(B)** Ni 2p, **(C)** P 2p, and **(D)** S 2p. (I) NiP-S/γ-Al_2O_3-MgO; (II) MoP-S/γ-Al_2O_3-MgO; and (III) NiMoP-S/γ-Al_2O_3-MgO.

TABLE 3 | Atomic chemical composition of the Mo 3d, Ni 2p, P 2p, and S 2p regions in the Al_2O_3-MgO supported NiMo mixed phosphidic-sulphidic phase.

Catalyst	Mo $3d_{5/2}$-$3d_{3/2}$			Ni $2p_{3/2}$-$2p_{1/2}$		S $2p_{3/2}$-$2p_{1/2}$		P $2p_{3/2}$-$2p_{1/2}$	
	$Mo^{\delta+}$ 228.7 eV (at %)	Mo^{4+} 229 eV (at %)	Mo^{6+} 232.5 eV (at %)	$Ni^{\delta+}$ 852.4 eV (at %)	Ni^{2+} 856 eV (at %)	S^{2-} 161.7 eV (at %)	SO_4^{2-} 168.9 eV (at %)	$P^{\delta+}$ 129.4 eV (at %)	P^{5+} 133.6 eV (at %)
NiP-S/γ-Al_2O_3-MgO				0.78	1.21	0.43	0.33	3.47	3.19
MoP-S/γ-Al_2O_3-MgO	1.72	0.82	1.02			0.50	0.26	3.45	3.21
NiMoP-S/γ-Al_2O_3-MgO	1.91	0.80	0.84	1.01	0.98	0.58	0.18	4.04	2.62

856, and 862 eV (Hsu and Lin, 2017). These signals are attributed to $Ni^{\delta+}$ ($0 < \delta + < 2$) of nickel phosphide, Ni^{2+} ions interacting with phosphate or sulfates, and the strong shake-up lines characteristic of Ni^{2+} species in an Ni-O-P/Ni-O-S matrix, respectively. Note that the electron binding energy of $Ni^{\delta+}$ was more extensive than that of metallic Ni, suggesting the charge transfer from Ni to P (Gonçalves et al., 2017). Likewise, **Figure 4A** shows the Mo $3d_{5/2\text{-}3/2}$ region spectra of MoP-S/γ-Al_2O_3-MgO and NiMoP-S/γ-Al_2O_3-MgO catalysts. The peaks confirm the presence on the surface of $Mo^{\delta+}$($0 < \delta + < 2$; Mo $3d_{5/2}$ = 228.7eV), Mo^{4+} (Mo $3d_{5/2}$ = 229 eV), and Mo^{6+} (Mo $3d_{5/2}$ = 232.5 eV) species due to Mo-P, MoS_2, and MoO_3, respectively (Phillips et al., 2002). It can be observed that the presence of a promoter is reflected in a higher amount of $Mo^{\delta+}$ and Mo^{4+} species (sulfided). Additionally, in the Mo $3d_{5/2\text{-}3/2}$ region, a shoulder at 226.5 eV was found, corresponding to the 2 s signal of sulfur, which can be confirmed by the presence of two bands in the S $2p_{3/2}$ region (Weber et al., 1996): a sign at 161.7 eV due to terminal disulfide and/or sulfide (S^{2-}) ligands in MoS_2 or NiMoS phases and the signal at 168.9 eV, which can be assigned to SO_4^{2-} (**Figure 4D**). The signals due to sulfur species and its proportion are much more important for MoP-S/γ-Al_2O_3-MgO and NiMoP-S/γ-Al_2O_3-MgO, whereas that partial S substitution of P in NiP-S/γ-Al_2O_3-MgO was less as shown by Raman results. **Figure 4C** shows the XPS spectra in the P 2p region, revealing two kinds of phosphorus signals with different relative contents on all catalysts. The peaks at 129.3 and 134.2 eV correspond to the reduced P species in the phosphides and the PO_4^{3-} species that were probably derived from the surface passivation (Sawhill et al., 2005). The binding energy of reduced P species is smaller than the element P, indicating that there is a charge transfer from Ni or Mo to P.

Curve fitting of the spectra in the P 2p region revealed that the amount of PO_4^{3-} species was much less than that of the reduced P (**Table 3**). This further demonstrates that more P atoms interacted with Ni or Mo atoms. Hence, the relative

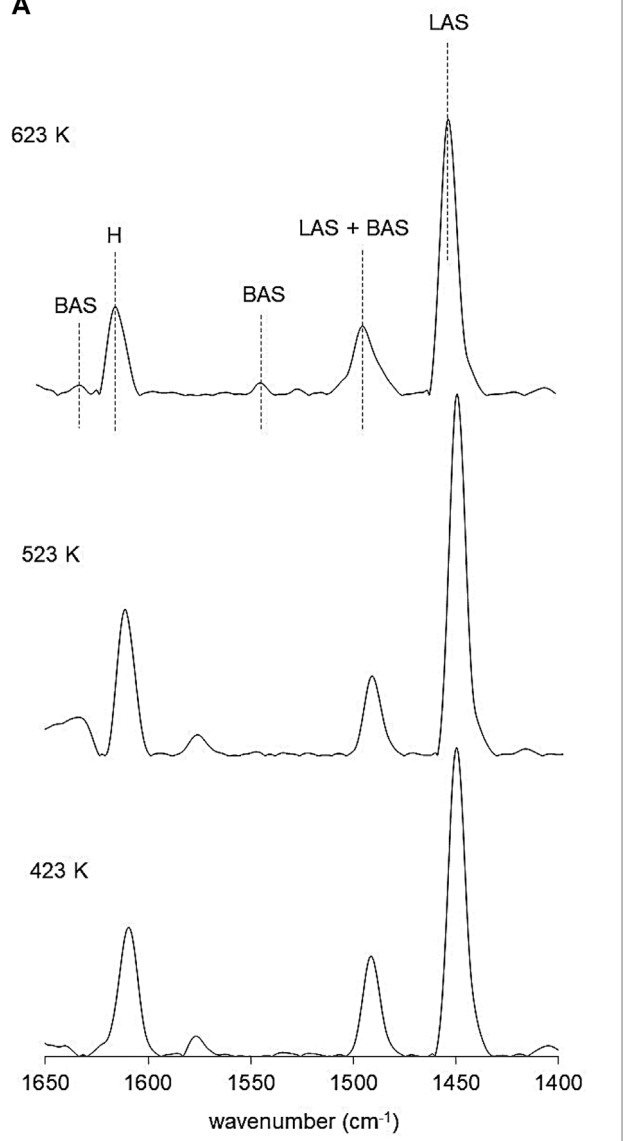

FIGURE 5 | (A) FTIR spectra of pyridine adsorption over the NiP-S/γ-Al_2O_3-MgO catalyst. **(B)** FTIR spectra of pyridine adsorption over the NiMoP-S/γ-Al_2O_3-MgO catalyst.

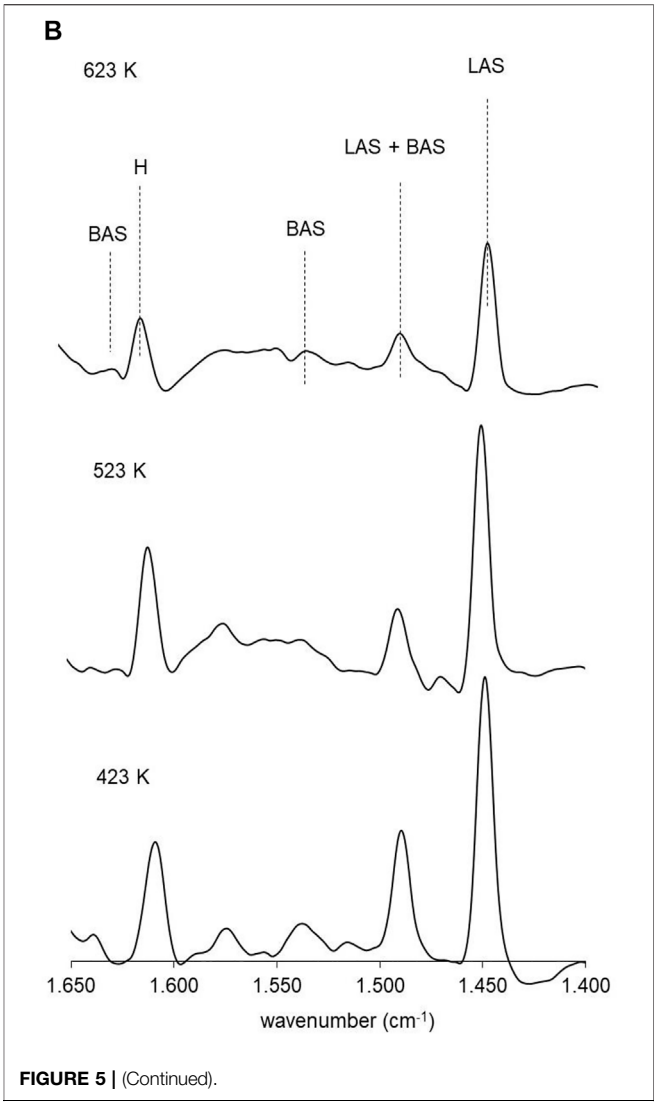

FIGURE 5 | (Continued).

quantities of low oxidation state Mo, Ni, P, and S species was higher in NiMoP-S/γ-Al_2O_3-MgO, suggesting a synergistic effect between the metals by the enhanced charge transfer from metals to P.

FTIR of Adsorbed Pyridine

Figures 5A,B present the infrared spectra in the region between 1,700 and 1,400 cm^{-1} of the pyridine vibration bands vs. thermodesorption temperature for NiP-S/γ-Al_2O_3-MgO and NiMoP-S/γ-Al_2O_3-MgO activated at 423, 523, and 623 K. This method was used to identify the types and strength of acid sites in the different materials (Crépeau et al., 2006). **Figure 5** shows bands at 1,450, 1,540/1,638, 1,490, and 1,608 cm^{-1}, attributed to pyridine bound to Lewis acid sites, Brönsted acid sites, the sum of Brönsted and Lewis acid sites, and hydrogen bonding with Al_2O_3 surface hydroxyl groups, respectively (Barzetti et al., 1996). This figure shows that the Lewis acid is dominant over the Brönsted acid for all the catalysts, as reported by Oyama (Lee and Oyama, 2006). The NiMoP-S/γ-Al_2O_3-MgO catalyst has a more significant number of Brønsted and Lewis sites as follows: 423 K (BS = 34.2 μmol/g and LS = 106.6 μmol/g), 523 K (BS = 15.2 μmol/g and LS = 89.8 μmol/g), and 623 K (BS = 15.7 μmol/g and LS = 36.9 μmol/g). However, as the temperature increases, it is observed that the amount of the Lewis sites in NiMoP-S/γ-Al_2O_3-MgO was much less than that of NiP-S/γ-Al_2O_3-MgO [423 K (BS = 1.4 μmol/g and LS = 94.7 μmol/g), 523 K (BS = 1.0 μmol/g and LS = 61.9 μmol/g), and 623 K (BS = 0.9 μmol/g and LS = 57.7 μmol/g)], suggesting that these sites in the NiP-S/γ-Al_2O_3-MgO catalyst are stronger that NiMoP-S/γ-Al_2O_3-MgO; moreover, their Brönsted acid sites did not produce appreciable changes (Ledesma et al., 2020). On the other hand,

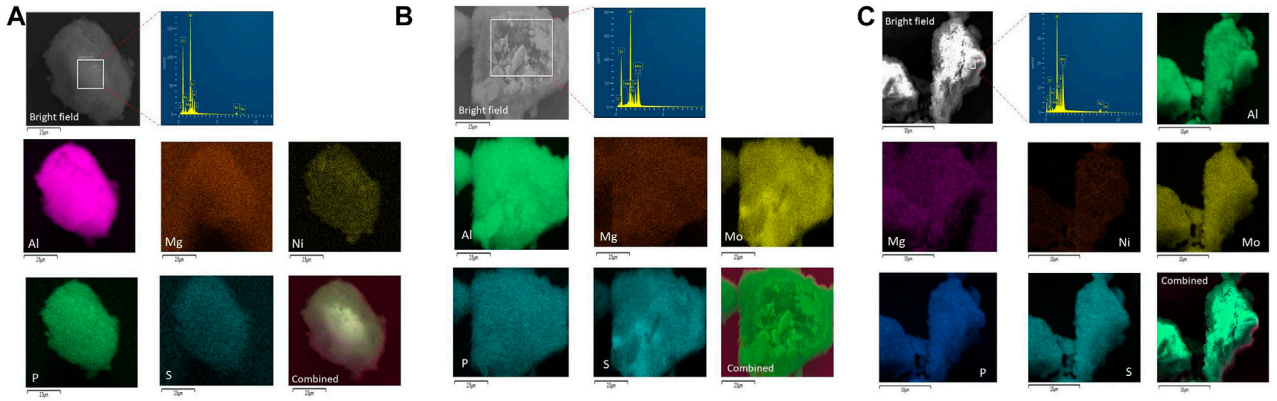

FIGURE 6 | (A) EDX elemental mapping of Ni, Al, O, P, Mg, and S over the NiP-S/γ-Al_2O_3-MgO catalyst. **(B)** EDX elemental mapping of Mo, Ni, Al, O, P, Mg, and S over the MoP-S/γ-Al_2O_3-MgO catalyst. **(C)** EDX elemental mapping of Mo, Ni, Al, O, P, Mg, and S over the NiMoP-S/γ-Al_2O_3-MgO catalyst.

TABLE 4 | Apparent rate constants and adsorption constants of the Al_2O_3-MgO supported NiMo mixed phosphidic-sulphidic phase for oleic and stearic acids hydrogenation in the reaction network shown in **Scheme 1**.

Catalyst	Fatty acids HYD rate constants × 10^3 mol/(g_{cat}·h)							Fatty acids HYD adsorption constants L/mol		Fatty acids HYD activities mol/(g_{cat}·h)		
	k_1	k_2	k_3	k_4	k_5	k_6	k_7	K_1	K_2	HDO	DCx-DCn	HCK
NiP-S/γ-Al_2O_3-MgO	5.1	2.3	3.7	3.6	44.7	4.5	1.8	2.51	6.46	9	45	6
MoP-S/γ-Al_2O_3-MgO	7.2	2.7	16.2	45.6	29.1	2.3	0.16	0.08	0.03	53	29	2
NiMoP-S/γ-Al_2O_3-MgO	0.31	4.0	12.4	46.7	40.9	2.4	0.036	0.25	0.45	47	41	2

HDO = k1 + k4, DCx-DCn = k5, HCK = k6 + k7.

the presence of Mo increased the content of Brönsted acid sites; then it is possible to presume that the MoP-S/γ-Al_2O_3-MgO catalyst will have a more significant number of Brönsted acid sites than NiP-S/γ-Al_2O_3-MgO.

SEM Analysis With Energy Dispersive X-Ray Spectroscopy and Elemental Mapping

Figures 6B,C exhibit the SEM microscopy of the MoP-S/γ-Al_2O_3-MgO and NiMoP-S/γ-Al_2O_3-MgO catalysts, which showed morphologies consisting of particle cumulus with irregular geometries, except for NiP-S/γ-Al_2O_3-MgO (**Figure 6A**), which presented a morphology regular with particle sizes smaller than NiMoP-S/γ-Al_2O_3-MgO and MoP-S/γ-Al_2O_3-MgO. The EDS elemental mapping confirmed the well-distributed presence of the atoms constituting the catalysts on the support, i.e., Mo, Ni, Al, O, P, Mg, and S. However, the micrographs show the greater intensity of mapping in a few catalyst zones for Ni and Mo atoms associated to the solubility of the precursors, suggesting that some of these atoms could precipitate. But they are not dispersing on the whole selected area forming a metal rich-aggregate "cluster" in the NiP-S/γ-Al_2O_3-MgO and MoP-S/γ-Al_2O_3-MgO catalysts (Puello-Polo et al., 2020).

Catalytic Tests

The fatty acids HYD activities function of the product conversion of the NiP-S/γ-Al_2O_3-MgO, MoP-S/γ-Al_2O_3-MgO, and NiMoP-S/γ-Al_2O_3-MgO catalysts are reported after 6 h of reaction in **Table 4**. The catalysts did not show significant differences in the transformations of oleic and stearic acids (~95%–99%), except in the conversion of stearic acid by NiP-S/γ-Al_2O_3-MgO (85%) as seen from **Figures 7A–C**, where the hydrogenation conversion of oleic acid to stearic acid was similar over the three catalysts; however, the HYD rate constant (k_3) for catalyst NiP-S/γ-Al_2O_3-MgO was much lower than that for other catalysts, which must be related to the oxophilic capacity of molybdenum (Zhang et al., 2020). Hence, the effect was evaluated on the performance of the HDO, HDCx-HDCn, and HCK activities (**Table 4**). The pseudo-first-order rate constant values [k_1+k_4 (HDO), k_5 (HDCx-HDCn) and k_6+k_7 (HCK)] of **Scheme 1** showed that MoP-S/γ-Al_2O_3-MgO was more active at HDO, showing the highest production rate for octadecane of 53 mol/(g_{cat}·h), whereas NiP-S/γ-Al_2O_3-MgO was more active at HDCx-HDCn [45 mol/(g_{cat}·h)] and HCK [6 mol/(g_{cat}·h)], and NiMoP-S/γ-Al_2O_3-MgO had a mix of HDO [47 mol/(g_{cat}·h)] and HDCx-HDCn [41 mol/(g_{cat}·h)], which showed production towards octadecane, heptadecane, and light hydrocarbons (**Figures 7A–C**). Likewise, MoP-S/γ-Al_2O_3-MgO and NiMoP-S/γ-Al_2O_3-MgO showed the highest HYD

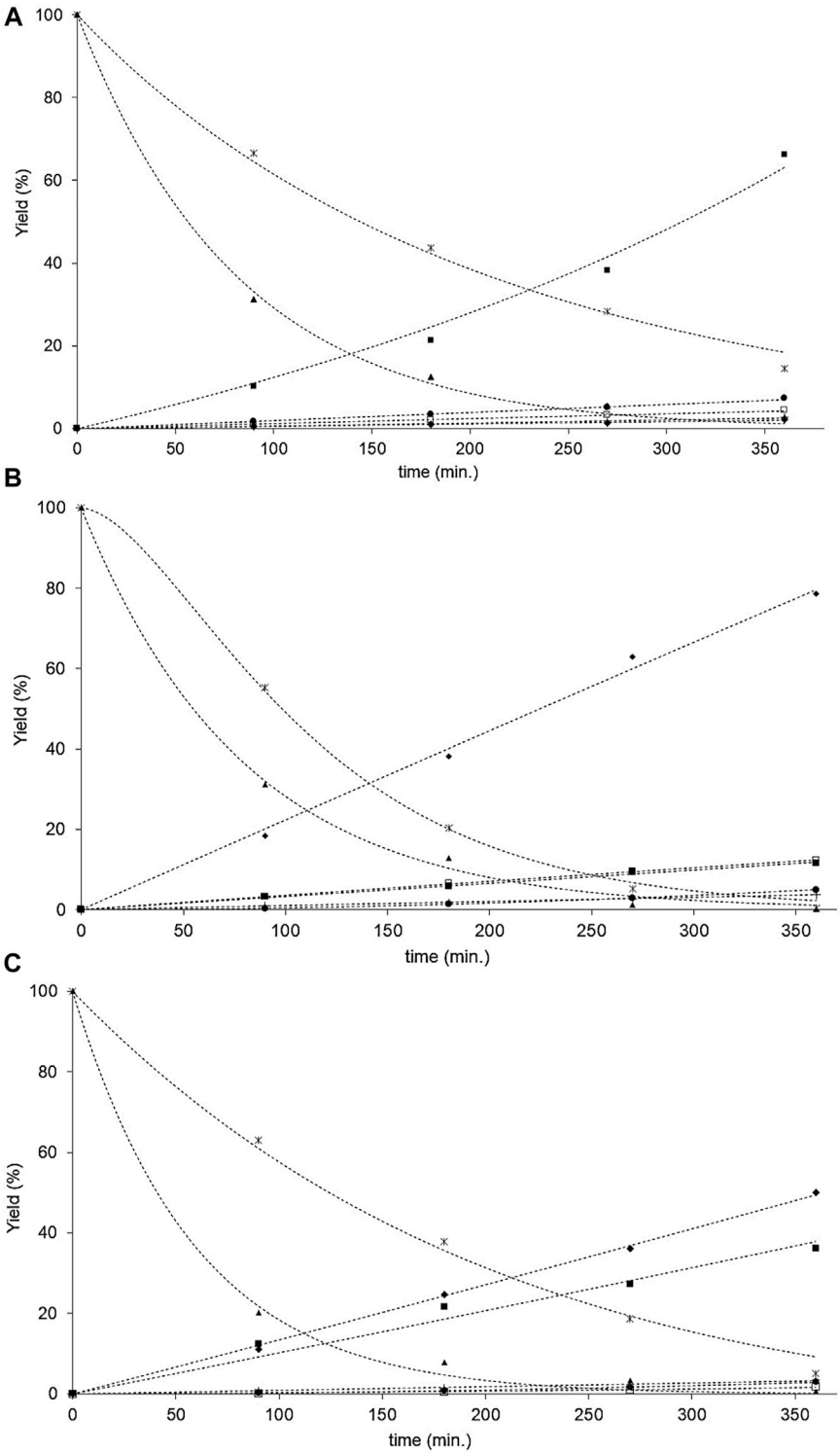

FIGURE 7 | (A) The oleic and stearic acids HYD activities in function of reaction time over the NiP-S/γ-Al_2O_3-MgO catalyst. (▲) Oleic acid, (ж) stearic acid, (□) 8-octadecene, (■) heptadecane, (◆) octadecane, (+) light HC, and (●) 8-methyl, 8-heptadecene. (---) predicted value. **(B)** The oleic and stearic acids HYD activities in function of reaction time over the MoP-S/γ-Al_2O_3-MgO catalyst. (▲) Oleic acid, (ж) stearic acid, (□) 8-octadecene, (■) heptadecane, (◆) octadecane, (+) light HC, and (●) 8-methyl, 8-heptadecene. (---) predicted value. **(C)** The oleic and stearic acids HYD activities in function of reaction time over the NiMoP-S/γ-Al_2O_3-MgO catalyst. (▲) Oleic acid, (ж) stearic acid, (□) 8-octadecene, (■) heptadecane, (◆) octadecane, (+) light HC, and (●) 8-methyl, 8-heptadecene. (---) predicted value.

from oleic acid to stearic acid of 16.2 and 12.4 mol/(g_{cat}·h), respectively. Therefore, the previous results confirm that MoP-S/γ-Al_2O_3-MgO and NiMoP-S/γ-Al_2O_3-MgO catalysts had a higher percentage of the HDO route (Nelson et al., 2006); while NiP-S/γ-Al_2O_3-MgO displayed a significant increase for the HDCx-HDCn and HCK routes. On the other hand, although the hydrocracking of the C18 and C17 hydrocarbons also took place in all the catalysts, their selectivity was very low on all the catalysts, considering the rate constant values (k_6+k_7). Although the surface area and pore size (similar) did not directly correlate with the catalytic activity, the decreasing pore volume probably allows greater exposure of the active sites to the catalysis regardless of which route is taken. In this regard, the HDO, HDCx-HDCn, and HCK activities can be correlated with the number and nature of the active sites on the surface (Lewis and Brönsted sites).

In the case of our best catalyst, the higher HDO and HDCx-HDCn activities could be ascribed to the high hydrogenolysis capacity of $Mo^{\delta+}/Mo^{4+}$ (oxophilic metal as mentioned above) on the surface combined with Brönsted and Lewis acidity of the material that preferentially increases the rate of C-O bond cleavage reactions, i.e., NiMoP-S/γ-Al_2O_3-MgO and MoP-S/γ-Al_2O_3-MgO have a lot of Brönsted acid sites compared to NiP-S/γ-Al_2O_3-MgO. Thus, the molar ratio between the HDO and HDCx-HDCn (denoted as (k_4+k_1)/k_5 ratio) can represent the selectivity between the decarbonylation and HDO pathways (**Table 4** and **Scheme 1**). It was found that the HDO/HDCx-HDCn ratios were between 0.19 and 1.81 on all catalysts at 300°C, meaning that the oleic and stearic acids were deoxygenated mainly through the HDO pathway as follows: NiP-S/γ-Al_2O_3-MgO < NiMoP-S/γ-Al_2O_3-MgO < MoP-S/γ-Al_2O_3-MgO. The metal Mo possesses a high oxophilicity; namely, Lewis acid sites on MoP-MoS_2 [coordinatively unsaturated sites (CUS)] adsorb the oxygen favoring the activation and dissociation of C=O and C-O bonds by Brønsted acid sites, i.e., neighboring SH and/or OH groups as mentioned by Wang (Wang and Ozkan, 2005). However, NiP-S/γ-Al_2O_3-MgO, despite having many Lewis and Brønsted acid sites, showed low activity towards HDO (k_1 vs. k_3); this is probably due to the strength of the acid site and not to the number of $Ni^{\delta+}$ species. Chen and Ruinart reported that Ni-based catalysts such as Ni, Ni_2P, and Ni_3S_2 promote the decarbonylation/decarboxylation pathway (Chen et al., 2014b; Ruinart de Brimont et al., 2012). In this regard, our NiP-S/γ-Al_2O_3-MgO catalyst exhibited HDCx-HDCn as the predominant route, suggesting that HDCx-HDCn could be related to the absence of sulfides; which is consistent with our results of XPS and Raman for NiP-S/γ-Al_2O_3-MgO that does not present an Ni sulfide on the surface. While the XPS and Raman results of MoP-S/γ-Al_2O_3-MgO and NiMoP-S/γ-Al_2O_3-MgO showed the presence of sulfides. Thus, a synergistic effect between MoS2 on the surface and the phosphide (phosphidic-sulphidic composite) would be an accurate representation for the active phase in typical hydrotreating conditions in these materials (Nelson et al., 2006). Hence, even though the selectivity behavior is completely the same between the phosphides and conventional sulfidic catalysts for oleic and stearic acids (Kaluža et al., 2019), this result agrees well with the previous report by Shim et al. (2015), showing the possible deoxygenation reaction pathways of oleic acid. Similarly, Coumans and Hensen, (2017) have suggested that in the NiMo sulfide the catalyst surface contains different sites for direct HDO and DCx-DCn reactions. On the side of the phosphides and carbides, Ni phosphides tend to follow the route of DCx and DCn with excellent conversions of fatty acids (Zhang et al., 2016; Ruangudomsakul et al., 2021); but reflects an intrinsic activity significantly lower than those obtained in this research; whilst Yun et al. (2017) reported that for NiMoP catalysts, Ni sites governed catalytic activity and Mo sites controlled the selectivity; however, our study shows that Ni tends to the route of DCx and DCn, and Mo the HDO. This is possibly because the phosphidic-sulphidic mixed-phase samples may have different active sites, which can improve DCx-DCn and HDO performance of catalysts.

To sum up, the catalytic activity obtained in HDO, HDC, and HCK may be correlated with the presence at the surface of Mo and Ni species, hence $Mo^{\delta+}$-Mo^{4+} in MoP-S/γ-Al_2O_3-MgO and $Ni^{\delta+}$ in NiP-S/γ-Al_2O_3-MgO favors HDO and DCx-DCn, respectively; hence the combination of $Mo^{\delta+}$-Mo^{4+} and $Ni^{\delta+}$ species in NiMoP-S/γ-Al_2O_3-MgO increases HDO and DCx-DCn; while for HCK, the Ni species have the most significant effect because MoP-S/γ-Al_2O_3-MgO and NiMoP-S/γ-Al_2O_3-MgO are less active towards HCK.

Determining the adsorption constants for the oleic and stearic acids HYD in the proposed mechanism could help us understand the different activities between the NiP-S/γ-Al_2O_3-MgO, MoP-S/γ-Al_2O_3-MgO, and NiMoP-S/γ-Al_2O_3-MgO catalysts. The data correlation is shown in **Figures 7A–C**, comparing experimental versus predicted yield. We found in the kinetic analysis that using the rate expressions Z = 2 for the inhibition terms gave better fitting to the data. Differences may rationalize this among reactions taking place in the HYD network of fatty acids, and based on our results, this leads us to think that there are two types of "bifunctional" sites (Infantes-Molina et al., 2015; Lee and Oyama, 2006). Therefore, we could designate, according to **Scheme 1**, a site (S1) for oleic acids and a site (S2) for stearic acids, where the hydrogenation (HYD) and HYG can occur in either of these two sites (BRIM and CUS sites, i.e., Lewis and Brønsted acid sites). At site 1, the oleic acid can be hydrogenated and hydrodeoxygenated to stearic acid and 8-octadecene, and the latter is subsequently isomerized to 8-methyl, 8-heptadecene. At the same time, site 2 stearic acid can be hydrodecarboxylated and hydrodeoxygenation to heptadecane and octadecane, which are hydrogenated to form low molecular weight compounds called here light hydrocarbons. In addition to this type of bifunctional site, the acid strength and number give preponderance to the proportion generated for each reaction route. Hence, the adsorption constants increase, for all the catalysts, in the following order: MoP-S/γ-Al_2O_3-MgO < NiMoP-S/γ-Al_2O_3-MgO < NiP-S/γ-Al_2O_3-MgO.

The difference between the adsorption constants found applying this model suggests that the strength and number of Lewis sites in NiP-S/γ-Al2O3-MgO cause a high adsorption strength of the fatty acids on the catalyst surface (XPS results do

not show sulfur species); otherwise it is observed in MoP-S/γ-Al_2O_3-MgO and NiMoP-S/γ-Al_2O_3-MgO. It seems that there is a type of synergism between the Lewis and Brönsted sites of the catalyst that achieves an optimal strength of the bond between the relevant intermediate and the catalyst as exposed in the classical Sabatier principle, which states that there is an optimum "bond strength" defining the best catalyst for a given reaction (Medford et al., 2015). We consider that phosphide acts as a structural promoter in the catalysts with sulfide species on the surface and a kind of synergism is present in the phosphidic-sulphidic mixed-phase, allowing the largest generation of heptadecane and octadecane by BRIM sites for HYD and CUS sites for HYG.

CONCLUSION

The effect of phosphidic-sulphidic phase content in MoP-S/γ-Al_2O_3-MgO, NiMoP-S/γ-Al_2O_3-MgO, and NiP-S/γ-Al_2O_3-MgO on hydrogenation of fatty acids was evaluated. The chemical analyses by FRX for MoP-S/γ-Al_2O_3-MgO, NiMoP-S/γ-Al_2O_3-MgO, and NiP-S/γ-Al_2O_3-MgO showed stoichiometric values for Al:Mg, Ni:Mo, Ni:P, and Mo:Ni:P of 38 and ~1, while EDS spectra and elemental mapping confirmed the presence of Mo, Ni, Al, O, P, Mg, and S with good distribution on Al_2O_3-MgO. The XRD patterns revealed differences between metallic phosphates and the phosphidic-sulphidic phase. However, it was difficult to distinguish a phosphide phase because the crystallite size was too small, and the phosphide particles were well dispersed on the support. MoP-S/γ-Al_2O_3-MgO and NiMoP-S/γ-Al_2O_3-MgO showed two typical Raman peaks at 380 and 405 cm^{-1} for the E^1_{2g} and A_{1g} active modes characteristic of the bulk of multilayered MoS_2. All the N_2 physisorption isotherms of the materials were type IV with H1 and H2 hysteresis loops. MoP-S/γ-Al_2O_3-MgO and NiP-S/γ-Al_2O_3-MgO showed better textural properties than NiMoP-S/γ-Al_2O_3-MgO with an average pore radius between 6.5 and 11.2 nm. XPS evidenced $Mo^{\delta+}$($0 < \delta+ < 2$), Mo^{4+}, Mo^{6+}, $Ni^{\delta+}$($0 < \delta+ < 2$), Ni^{2+}, $P^{\delta+}$, and P^{5+} species, which showed a dependence with the type of metal and the presence of sulfur. The FTIR Py analysis of MoP-S/γ-Al_2O_3-MgO, NiMoP-S/γ-Al_2O_3-MgO, and NiP-S/γ-Al_2O_3-MgO showed the main band characteristics of the pyridine adsorbed on Lewis acid sites and much lower amounts of Brønsted acid sites. The NiMoP-S/γ-Al_2O_3-MgO catalyst had a more significant number of Brønsted and Lewis sites (15.7–34.2 μmol/g vs. 36.9–106.6 μmol/g). However, the Lewis sites in NiP-S/γ-Al_2O_3-MgO were stronger that NiMoP-S/γ-Al_2O_3-MgO. MoP-S/γ-Al_2O_3-MgO was more active at HDO showing the highest production rate for octadecane of 53 mol/(g_{cat}·h), whereas NiP-S/γ-Al_2O_3-MgO was more active at HDCx-HDCn [45 mol/(g_{cat}·h)] and HCK [6 mol/(g_{cat}·h)], and NiMoP-S/γ-Al_2O_3-MgO had a mix of HDO [47 mol/(g_{cat}·h)] and HDCx-HDCn [41 mol/(g_{cat}·h)]. The higher HDO and HDCx-HDCn activities could be ascribed to the high hydrogenolysis capacity of molybdenum sulfide (oxophilic metal). The $(k_4+k_1)/k_5$ ratios were between 0.19 and 1.81 on all catalysts at 300°C, meaning that the oleic and stearic acids were deoxygenated mainly through the HDO pathway as follows: NiP-S/γ-Al_2O_3-MgO < NiMoP-S/γ-Al_2O_3-MgO < MoP-S/γ-Al_2O_3-MgO. The catalysts had bifunctional sites, leading to an increase of the adsorption constants as follows: MoP-S/γ-Al_2O_3-MgO (K_1 = 0.08 and K_2 = 0.03 L/mol) < NiMoP-S/γ-Al_2O_3-MgO (K_1 = 0.25 and K_2 = 0.45 L/mol) < NiP-S/γ-Al_2O_3-MgO (K_1 = 2.5 and K_2 = 6.5 L/mol). Hence the high production of heptadecane and octadecane by the presence of mixed NiMo phosphidic-sulphidic species (BRIM sites for HYD and CUS sites for HYG) suggests a type of synergism between the Lewis and Brönsted sites of the catalyst giving an optimum "bond strength" defining the best catalyst for a given reaction.

DATA AVAILABILITY STATEMENT

The original contributions presented in the study are included in the article/Supplementary Material, further inquiries can be directed to the corresponding author.

AUTHOR CONTRIBUTIONS

Introduction, EP-P and DA; experimental, EP-P, EM, and DA.; results and discussion, and conclusion, EP-P, EM, and DA; investigation, EP-P, EM and DA; resources, EP-P and EM; writing—original draft preparation, EP-P, EM, and DA; writing—review and editing, EP-P and EM; supervision, EP-P and EM; project administration, EP-P and EM.

FUNDING

Universidad del Atlántico, Projects CB40-TGI2018/CB39-TGI2018 and Universidad del Norte, GRANTS 2019-17.

ACKNOWLEDGMENTS

The authors would like to acknowledge financial support by Universidad del Atlántico and Universidad del Norte, and the fine technical assistance of Catalysis Research Center-CICAT UIS. EP-P is grateful to Ofelia Polo, and Jonathan Romero for technical assistance.

REFERENCES

Arend, M., Nonnen, T., Hoelderich, W. F., Fischer, J., and Groos, J. (2011). Catalytic Deoxygenation of Oleic Acid in Continuous Gas Flow for the Production of Diesel-like Hydrocarbons. *Appl. Catal. A General* 399 (1), 198–204. doi:10.1016/j.apcata.2011.04.004

Barrett, E. P., Joyner, L. G., and Halenda, P. P. (1951). The Determination of Pore Volume and Area Distributions in Porous Substances. I. Computations from Nitrogen Isotherms. *J. Am. Chem. Soc.* 73 (1), 373–380. doi:10.1021/ja01145a126

Barzetti, T., Selli, E., Moscotti, D., and Forni, L. (1996). Pyridine and Ammonia as Probes for FTIR Analysis of Solid Acid Catalysts. *Faraday Trans.* 92 (8), 1401. doi:10.1039/ft9969201401

Berenguer, A., Sankaranarayanan, T. M., Gómez, G., Moreno, I., Coronado, J. M., Pizarro, P., et al. (2016). Evaluation of Transition Metal Phosphides Supported on Ordered Mesoporous Materials as Catalysts for Phenol Hydrodeoxygenation. *Green Chem.* 18 (7), 1938–1951. doi:10.1039/C5GC02188J

Bezergianni, S., and Dimitriadis, A. (2013). Comparison between Different Types of Renewable Diesel. *Renew. Sustain. Energy Rev.* 21, 110–116. doi:10.1016/j.rser.2012.12.042

Botto, I. L., Garcia, A. C., and Thomas, H. J. (1992). Spectroscopical Approach to Some Heteropolymolybdates with the Anderson Structure. *J. Phys. Chem. Solids* 53 (8), 1075–1080. doi:10.1016/0022-3697(92)90081-N

Bui, P., Cecilia, J. A., Oyama, S. T., Takagaki, A., Infantes-Molina, A., Zhao, H., et al. (2012). Studies of the Synthesis of Transition Metal Phosphides and Their Activity in the Hydrodeoxygenation of a Biofuel Model Compound. *J. Catal.* 294, 184–198. doi:10.1016/j.jcat.2012.07.021

Butt, G., Sammes, N., Tompsett, G., Smirnova, A., and Yamamoto, O. (2004). Raman Spectroscopy of Superionic Ti-Doped Li3Fe2(PO4)3 and LiNiPO4 Structures. *J. Power Sources* 134 (1), 72–79. doi:10.1016/j.jpowsour.2004.01.053

Cecilia, J. A., Infantes-Molina, A., Rodríguez-Castellón, E., Jiménez-López, A., and Oyama, S. T. (2013). Oxygen-removal of Dibenzofuran as a Model Compound in Biomass Derived Bio-Oil on Nickel Phosphide Catalysts: Role of Phosphorus. *Appl. Catal. B Environ.* 136-137, 140–149. doi:10.1016/j.apcatb.2013.01.047

Centeno, A., Laurent, E., and Delmon, B. (1995). Influence of the Support of CoMo Sulfide Catalysts and of the Addition of Potassium and Platinum on the Catalytic Performances for the Hydrodeoxygenation of Carbonyl, Carboxyl, and Guaiacol-type Molecules. *J. Catal.* 154 (2), 288–298. doi:10.1006/jcat.1995.1170

Chen, J., Shi, H., Li, L., and Li, K. (2014). Deoxygenation of Methyl Laurate as a Model Compound to Hydrocarbons on Transition Metal Phosphide Catalysts. *Appl. Catal. B Environ.* 144, 870–884. doi:10.1016/j.apcatb.2013.08.026

Chen, J., Yang, Y., Shi, H., Li, M., Chu, Y., Pan, Z., et al. (2014). Regulating Product Distribution in Deoxygenation of Methyl Laurate on Silica-Supported Ni-Mo Phosphides: Effect of Ni/Mo Ratio. *Fuel* 129, 1–10. doi:10.1016/j.fuel.2014.03.049

Cho, A., Shin, J., Takagaki, A., Kikuchi, R., and Oyama, S. T. (2012). Ligand and Ensemble Effects in Bimetallic NiFe Phosphide Catalysts for the Hydrodeoxygenation of 2-Methyltetrahydrofuran. *Top. Catal.* 55 (14-15), 969–980. doi:10.1007/s11244-012-9882-3

Coumans, A. E., and Hensen, E. J. M. (2017). A Model Compound (Methyl Oleate, Oleic Acid, Triolein) Study of Triglycerides Hydrodeoxygenation over Alumina-Supported NiMo Sulfide. *Appl. Catal. B Environ.* 201, 290–301. doi:10.1016/j.apcatb.2016.08.036

Crépeau, G., Montouillout, V., Vimont, A., Mariey, L., Cseri, T., and Maugé, F. (2006). Nature, Structure and Strength of the Acidic Sites of Amorphous Silica Alumina: An IR and NMR Study. *J. Phys. Chem. B* 110 (31), 15172–15185. doi:10.1021/jp062252d

Donnis, B., Egeberg, R. G., Blom, P., and Knudsen, K. G. (2009). Hydroprocessing of Bio-Oils and Oxygenates to Hydrocarbons. Understanding the Reaction Routes. *Top. Catal.* 52 (3), 229–240. doi:10.1007/s11244-008-9159-z

Duan, Y. (2017). Synthesis of Renewable Diesel Range Alkanes by Hydrodeoxygenation of Palmitic Acid over 5% Ni/CNTs under Mild Conditions. *Catalysts* 7 (12), 81. doi:10.3390/catal7030081

Emeis, C. A. (1993). Determination of Integrated Molar Extinction Coefficients for Infrared Absorption Bands of Pyridine Adsorbed on Solid Acid Catalysts. *J. Catal.* 141 (2), 347–354. doi:10.1006/jcat.1993.1145

Farojr, A., and Dossantos, A. (2006). Cumene Hydrocracking and Thiophene HDS on Niobia-Supported Ni, Mo and Ni-Mo Catalysts. *Catal. Today* 118 (3), 402–409. doi:10.1016/j.cattod.2006.07.027

Feitosa, L. F., Berhault, G., Laurenti, D., Davies, T. E., and Teixeira da Silva, V. (2016). Synthesis and Hydrodeoxygenation Activity of Ni2P/C - Effect of the Palladium Salt on Lowering the Nickel Phosphide Synthesis Temperature. *J. Catal.* 340, 154–165. doi:10.1016/j.jcat.2016.05.016

Ferdous, D., Dalai, A. K., and Adjaye, J. (2004). A Series of NiMo/Al2O3 Catalysts Containing Boron and Phosphorus. *Appl. Catal. A General* 260 (2), 137–151. doi:10.1016/j.apcata.2003.10.010

Froment, G. F., De Wilde, J., and Bischoff, K. B. (2011). *Chemical Reactor Analysis and Design*. 3rd ed. Hoboken, N.J: Wiley.

Gonçalves, V. O. O., de Souza, P. M., Cabioc'h, T., da Silva, V. T., Noronha, F. B., and Richard, F. (2017). Hydrodeoxygenation of M-Cresol over Nickel and Nickel Phosphide Based Catalysts. Influence of the Nature of the Active Phase and the Support. *Appl. Catal. B Environ.* 219, 619–628. doi:10.1016/j.apcatb.2017.07.042

Gosselink, R. W., Hollak, S. A. W., Chang, S.-W., van Haveren, J., de Jong, K. P., Bitter, J. H., et al. (2013). Reaction Pathways for the Deoxygenation of Vegetable Oils and Related Model Compounds. *ChemSusChem* 6 (9), 1576–1594. doi:10.1002/cssc.201300370

Gousi, M., Andriopoulou, C., Bourikas, K., Ladas, S., Sotiriou, M., Kordulis, C., et al. (2017). Green Diesel Production over Nickel-Alumina Co-precipitated Catalysts. *Appl. Catal. A General* 536, 45–56. doi:10.1016/j.apcata.2017.02.010

Guan, Q., Wan, F., Han, F., Liu, Z., and Li, W. (2016). Hydrodeoxygenation of Methyl Palmitate over MCM-41 Supported Nickel Phosphide Catalysts. *Catal. Today* 259, 467–473. doi:10.1016/j.cattod.2015.03.010

Hachemi, I., and Murzin, D. Y. (2018). Kinetic Modeling of Fatty Acid Methyl Esters and Triglycerides Hydrodeoxygenation over Nickel and Palladium Catalysts. *Chem. Eng. J.* 334, 2201–2207. doi:10.1016/j.cej.2017.11.153

Han, J., Duan, J., Chen, P., Lou, H., Zheng, X., and Hong, H. (2012). Carbon-Supported Molybdenum Carbide Catalysts for the Conversion of Vegetable Oils. *ChemSusChem* 5 (4), 727–733. doi:10.1002/cssc.201100476

Helwani, Z., Othman, M. R., Aziz, N., Fernando, W. J. N., and Kim, J. (2009). Technologies for Production of Biodiesel Focusing on Green Catalytic Techniques: A Review. *Fuel Process. Technol.* 90 (12), 1502–1514. doi:10.1016/j.fuproc.2009.07.016

Hsu, P.-J., and Lin, Y.-C. (2017). Hydrodeoxygenation of 4-methylguaiacol over Silica-Supported Nickel Phosphide Catalysts: The Particle Size Effect. *J. Taiwan Inst. Chem. Eng.* 79, 80–87. doi:10.1016/j.jtice.2017.02.020

Immer, J. G., Kelly, M. J., and Lamb, H. H. (2010). Catalytic Reaction Pathways in Liquid-phase Deoxygenation of C18 Free Fatty Acids. *Appl. Catal. A General* 375 (1), 134–139. doi:10.1016/j.apcata.2009.12.028

Infantes-Molina, A., Gralberg, E., Cecilia, J. A., Finocchio, E., and Rodríguez-Castellón, E. (2015). Nickel and Cobalt Phosphides as Effective Catalysts for Oxygen Removal of Dibenzofuran: Role of Contact Time, Hydrogen Pressure and Hydrogen/feed Molar Ratio. *Catal. Sci. Technol.* 5 (6), 3403–3415. doi:10.1039/C5CY00282F

International Centre for Diffraction Data (1995). *International Centre for Diffraction Data® (ICDD®), Power Diffraction File, ICDD*. Philadelphia: Newtown Square Philadelphia.

Kaluža, L., Karban, J., and Gulková, D. (2019). Activity and Selectivity of Co(Ni)Mo Sulfides Supported on MgO, Al2O3, ZrO2, TiO2, MCM-41 and Activated Carbon in Parallel Hydrodeoxygenation of Octanoic Acid and Hydrodesulfurization of 1-benzothiophene. *Reac Kinet. Mech. Cat.* 127 (2), 887–902. doi:10.1007/s11144-019-01620-x

Kamal-Eldin, A., and Yanishlieva, N. V. (2002). N-3 Fatty Acids for Human Nutrition: Stability Considerations. *Eur. J. Lipid Sci. Technol.* 104 (12), 825–836. doi:10.1002/1438-9312(200212)104:12<825::AID-EJLT825>3.0.CO;2-N

Kandel, K., Anderegg, J. W., Nelson, N. C., Chaudhary, U., and Slowing, I. I. (2014). Supported Iron Nanoparticles for the Hydrodeoxygenation of Microalgal Oil to Green Diesel. *J. Catal.* 314, 142–148. doi:10.1016/j.jcat.2014.04.009

Khzouz, M., Wood, J., Pollet, B., and Bujalski, W. (2013). Characterization and Activity Test of Commercial Ni/Al2O3, Cu/ZnO/Al2O3 and Prepared Ni-Cu/Al2O3 Catalysts for Hydrogen Production from Methane and Methanol Fuels. *Int. J. Hydrogen Energy* 38 (3), 1664–1675. doi:10.1016/j.ijhydene.2012.07.026

Klicpera, T., and Zdražil, M. (2002). Preparation of High-Activity MgO-Supported Co-mo and Ni-Mo Sulfide Hydrodesulfurization Catalysts. *J. Catal.* 206 (2), 314–320. doi:10.1006/jcat.2001.3488

Klicpera, T., and Zdražil, M. (2000). Synthesis of a High Surface Area Monolayer MoO3/MgO Catalyst in a (NH4)6Mo7O24/MgO/methanol Slurry, and its Hydrodesulfurization Activity. *J. Mat. Chem.* 10 (7), 1603–1608. doi:10.1039/b001375g

Kubička, D., and Kaluža, L. (2010). Deoxygenation of Vegetable Oils over Sulfided Ni, Mo and NiMo Catalysts. *Appl. Catal. A General* 372 (2), 199–208. doi:10.1016/j.apcata.2009.10.034

Kumar, P., Yenumala, S. R., Maity, S. K., and Shee, D. (2014). Kinetics of Hydrodeoxygenation of Stearic Acid Using Supported Nickel Catalysts:

Effects of Supports. *Appl. Catal. A General* 471, 28–38. doi:10.1016/j.apcata.2013.11.021

Ledesma, B. C., Martínez, M. L., and Beltramone, A. R. (2020). Iridium-supported SBA-15 Modified with Ga and Al as a Highly Active Catalyst in the Hydrodenitrogenation of Quinoline. *Catal. Today* 349, 178–190. doi:10.1016/j.cattod.2018.04.061

Lee, Y., and Oyama, S. (2006). Bifunctional Nature of a SiO2-Supported Ni2P Catalyst for Hydrotreating: EXAFS and FTIR Studies. *J. Catal.* 239 (2), 376–389. doi:10.1016/j.jcat.2005.12.029

Leyva, C., Rana, M. S., Trejo, F., and Ancheyta, J. (2007). On the Use of Acid-Base-Supported Catalysts for Hydroprocessing of Heavy Petroleum. *Ind. Eng. Chem. Res.* 46 (23), 7448–7466. doi:10.1021/ie070128q

Li, H., Zhang, Q., Yap, C. C. R., Tay, B. K., Edwin, T. H. T., Olivier, A., et al. (2012). From Bulk to Monolayer MoS2: Evolution of Raman Scattering. *Adv. Funct. Mat.* 22 (7), 1385–1390. doi:10.1002/adfm.201102111

Li, J., Chai, Y., Liu, B., Wu, Y., Li, X., Tang, Z., et al. (2014). The Catalytic Performance of Ni2P/Al2O3 Catalyst in Comparison with Ni/Al2O3 Catalyst in Dehydrogenation of Cyclohexane. *Appl. Catal. A General* 469, 434–441. doi:10.1016/j.apcata.2013.09.047

Liu, X., Li, Z., Zhang, B., and Hu, M. (2017). Improvement of Hydrodeoxygenation Stability of Nickel Phosphide Based Catalysts by Silica Modification as Structural Promoter. *Fuel* 204, 144–151. doi:10.1016/j.fuel.2017.05.054

Medford, A. J., Vojvodic, A., Hummelshøj, J. S., Voss, J., Abild-Pedersen, F., Studt, F., et al. (2015). From the Sabatier Principle to a Predictive Theory of Transition-Metal Heterogeneous Catalysis. *J. Catal.* 328, 36–42. doi:10.1016/j.jcat.2014.12.033

Méndez, F. J., Bastardo-González, E., Betancourt, P., Paiva, L., and Brito, J. L. (2013). NiMo/MCM-41 Catalysts for the Hydrotreatment of Polychlorinated Biphenyls. *Catal. Lett.* 143 (1), 93–100. doi:10.1007/s10562-012-0933-y

Nelson, A., Sun, M., and Junaid, A. (2006). On the Structure and Composition of the Phosphosulfide Overlayer on Ni2P at Hydrotreating Conditions. *J. Catal.* 241 (1), 180–188. doi:10.1016/j.jcat.2006.04.023

Pan, Z., Wang, R., Li, M., Chu, Y., and Chen, J. (2015). Deoxygenation of Methyl Laurate to Hydrocarbons on Silica-Supported Ni-Mo Phosphides: Effect of Calcination Temperatures of Precursor. *J. Energy Chem.* 24 (1), 77–86. doi:10.1016/S2095-4956(15)60287-X

Patil, S. J., and Vaidya, P. D. (2018). On the Production of Bio-Hydrogenated Diesel over Hydrotalcite-like Supported Palladium and Ruthenium Catalysts. *Fuel Process. Technol.* 169, 142–149. doi:10.1016/j.fuproc.2017.09.026

Pearlson, M., Wollersheim, C., and Hileman, J. (2013). A Techno-Economic Review of Hydroprocessed Renewable Esters and Fatty Acids for Jet Fuel Production. *Biofuels, Bioprod. Bioref.* 7 (1), 89–96. doi:10.1002/bbb.1378

Phillips, D. C., Sawhill, S. J., Self, R., and Bussell, M. E. (2002). Synthesis, Characterization, and Hydrodesulfurization Properties of Silica-Supported Molybdenum Phosphide Catalysts. *J. Catal.* 207 (2), 266–273. doi:10.1006/jcat.2002.3524

Puello-Polo, E., and Brito, J. L. (2008). Effect of the Type of Precursor and the Synthesis Method on Thiophene Hydrodesulfurization Activity of Activated Carbon Supported Fe-Mo, Co-mo and Ni-Mo Carbides. *J. Mol. Catal. A Chem.* 281 (1), 85–92. doi:10.1016/j.molcata.2007.09.015

Puello-Polo, E., Marquez, E., and Brito, J. L. (2018). One-pot Synthesis of Nb-Modified Al2O3 Support for NiMo Hydrodesulfurization Catalysts. *J. Sol-Gel Sci. Technol.* 88 (1), 90–99. doi:10.1007/s10971-018-4792-x

Puello-Polo, E., Pájaro, Y., and Márquez, E. (2020). Effect of the Gallium and Vanadium on the Dibenzothiophene Hydrodesulfurization and Naphthalene Hydrogenation Activities Using Sulfided NiMo-V2O5/Al2O3-Ga2O3. *Catalysts* 10 (8), 894. doi:10.3390/catal10080894

Puello-Polo, E., Reales, Y. P., Marquez, E., Larruded, D. G., Arzuza, L. C. C., and Toloza, C. A. T. (2021). Effect of Gallium and Vanadium in NiMoV/Al2O3-Ga2O3 Catalysts on Indole Hydrodenitrogenation. *Catal. Lett.* 151 (7), 2038–2055. doi:10.1007/s10562-020-03438-y

Rensel, D. J., Rouvimov, S., Gin, M. E., and Hicks, J. C. (2013). Highly Selective Bimetallic FeMoP Catalyst for C-O Bond Cleavage of Aryl Ethers. *J. Catal.* 305, 256–263. doi:10.1016/j.jcat.2013.05.026

Ruangudomsakul, M., Osakoo, N., Keawkumay, C., Kongmanklang, C., Butburee, T., Kiatphuengporn, S., et al. (2021). Influential Properties of Activated Carbon on Dispersion of Nickel Phosphides and Catalytic Performance in Hydrodeoxygenation of Palm Oil. *Catal. Today* 367, 153–164. doi:10.1016/j.cattod.2020.04.068

Ruinart de Brimont, M., Dupont, C., Daudin, A., Geantet, C., and Raybaud, P. (2012). Deoxygenation Mechanisms on Ni-Promoted MoS2 Bulk Catalysts: A Combined Experimental and Theoretical Study. *J. Catal.* 286, 153–164. doi:10.1016/j.jcat.2011.10.022

Satterfield, C. N., Modell, M., and Wilkens, J. A. (1980). Simultaneous Catalytic Hydrodenitrogenation of Pyridine and Hydrodesulfurization of Thiophene. *Ind. Eng. Chem. Proc. Des. Dev.* 19 (1), 154–160. doi:10.1021/i260073a027

Sawhill, S., Layman, K., Vanwyk, D., Engelhard, M., Wang, C., and Bussell, M. (2005). Thiophene Hydrodesulfurization over Nickel Phosphide Catalysts: Effect of the Precursor Composition and Support. *J. Catal.* 231 (2), 300–313. doi:10.1016/j.jcat.2005.01.020

Shim, J.-O., Jeong, D.-W., Jang, W.-J., Jeon, K.-W., Kim, S.-H., Jeon, B.-H., et al. (2015). Optimization of Unsupported CoMo Catalysts for Decarboxylation of Oleic Acid. *Catal. Commun.* 67, 16–20. doi:10.1016/j.catcom.2015.03.034

Smirnov, A. A., Khromova, S. A., Ermakov, D. Y., Bulavchenko, O. A., Saraev, A. A., Aleksandrov, P. V., et al. (2016). The Composition of Ni-Mo Phases Obtained by NiMoOx-SiO2 Reduction and Their Catalytic Properties in Anisole Hydrogenation. *Appl. Catal. A General* 514, 224–234. doi:10.1016/j.apcata.2016.01.025

Solis, D., Klimova, T., Ramírez, J., and Cortez, T. (2004). NiMo/Al2O3-MgO (X) Catalysts: the Effect of the Prolonged Exposure to Ambient Air on the Textural and Catalytic Properties. *Catal. Today* 98 (1), 99–108. doi:10.1016/j.cattod.2004.07.024

Sotelo-Boyás, R., Liu, Y., and Minowa, T. (2011). Renewable Diesel Production from the Hydrotreating of Rapeseed Oil with Pt/Zeolite and NiMo/Al2O3 Catalysts. *Ind. Eng. Chem. Res.* 50 (5), 2791–2799. doi:10.1021/ie100824d

Souza Macedo, L., Oliveira, R. R., van Haasterecht, T., Teixeira da Silva, V., and Bitter, H. (2019). Influence of Synthesis Method on Molybdenum Carbide Crystal Structure and Catalytic Performance in Stearic Acid Hydrodeoxygenation. *Appl. Catal. B Environ.* 241, 81–88. doi:10.1016/j.apcatb.2018.09.020

Susanto, B. H., Prakasa, M. B., Nasikin, M., and Sukirno, S. (2016). Synthesis of Renewable Diesel from Palm Oil and Jatropha Curcas Oil through Hydrodeoxygenation Using NiMo/Zal. *IJTech* 7 (8), 1404. doi:10.14716/ijtech.v7i8.6886

Thommes, M., Kaneko, K., Neimark, A. V., Olivier, J. P., Rodriguez-Reinoso, F., Rouquerol, J., et al. (2015). Physisorption of Gases, with Special Reference to the Evaluation of Surface Area and Pore Size Distribution (IUPAC Technical Report). *Pure Appl. Chem.* 87 (9-10), 1051–1069. doi:10.1515/pac-2014-1117

Trejo, F., Ancheyta, J., Centeno, G., and Marroquín, G. (2005). Effect of Hydrotreating Conditions on Maya Asphaltenes Composition and Structural Parameters. *Catal. Today* 109 (1), 178–184. doi:10.1016/j.cattod.2005.08.013

Ueno, A., Suzuki, H., and Kotera, Y. (1983). Particle-size Distribution of Nickel Dispersed on Silica and its Effects on Hydrogenation of Propionaldehyde. *J. Chem. Soc. Faraday Trans. 1* 179 (1), 127. doi:10.1039/f19837900127

Uhlig, H., Muenster, T., Kloess, G., Ebbinghaus, S. G., Einicke, W.-D., Gläser, R., et al. (2018). Synthesis of MCM-48 Granules with Bimodal Pore Systems via Pseudomorphic Transformation of Porous Glass. *Microporous Mesoporous Mater.* 257, 185–192. doi:10.1016/j.micromeso.2017.08.033

Wang, F., Jiang, J., Wang, K., Zhai, Q., Sun, H., Liu, P., et al. (2018). Activated Carbon Supported Molybdenum and Tungsten Carbides for Hydrotreatment of Fatty Acids into Green Diesel. *Fuel* 228, 103–111. doi:10.1016/j.fuel.2018.04.150

Wang, W., Yang, Y., Luo, H., Hu, T., and Liu, W. (2011). Amorphous Co-mo-B Catalyst with High Activity for the Hydrodeoxygenation of Bio-Oil. *Catal. Commun.* 12 (6), 436–440. doi:10.1016/j.catcom.2010.11.001

Wang, X., Clark, P., and Oyama, S. T. (2002). Synthesis, Characterization, and Hydrotreating Activity of Several Iron Group Transition Metal Phosphides. *J. Catal.* 208 (2), 321–331. doi:10.1006/jcat.2002.3604

Wang, X., and Ozkan, U. S. (2005). Characterization of Active Sites over Reduced Ni–Mo/Al2O3 Catalysts for Hydrogenation of Linear Aldehydes. *J. Phys. Chem. B* 109 (5), 1882–1890. doi:10.1021/jp046489q

Wang, X., Zhao, Z., Zheng, P., Chen, Z., Duan, A., Xu, C., et al. (2016). Synthesis of NiMo Catalysts Supported on Mesoporous Al2O3 with Different Crystal Forms and Superior Catalytic Performance for the Hydrodesulfurization of Dibenzothiophene and 4,6-dimethyldibenzothiophene. *J. Catal.* 344, 680–691. doi:10.1016/j.jcat.2016.10.016

Weber, T., Muijsers, J. C., van Wolput, J. H. M. C., Verhagen, C. P. J., and Niemantsverdriet, J. W. (1996). Basic Reaction Steps in the Sulfidation of Crystalline MoO3 to MoS2, as Studied by X-Ray Photoelectron and Infrared Emission Spectroscopy. *J. Phys. Chem.* 100 (33), 14144–14150. doi:10.1021/jp961204y

Yang, J.-H., Song, X., Zhao, X., Wang, Y., Yang, Y., and Gao, L. (2019). Nickel Phosphate Materials Regulated by Doping Cobalt for Urea and Methanol Electro-Oxidation. *Int. J. Hydrogen Energy* 44 (31), 16305–16314. doi:10.1016/j.ijhydene.2019.05.016

Yang, S., Li, C., Wang, Y., Chen, S., Cui, M., Bai, X., et al. (2020). Suppressing Surface Passivation of Bimetallic Phosphide by Sulfur for Long-Life Alkaline Aqueous Zinc Batteries. *Energy Storage Mater.* 33, 230–238. doi:10.1016/j.ensm.2020.08.005

Yang, Y., Gilbert, A., and Xu, C. (2009). Hydrodeoxygenation of Bio-Crude in Supercritical Hexane with Sulfided CoMo and CoMoP Catalysts Supported on MgO: A Model Compound Study Using Phenol. *Appl. Catal. A General* 360 (2), 242–249. doi:10.1016/j.apcata.2009.03.027

Yang, Y., Ochoa-Hernández, C., de la Peña O'Shea, V. A., Coronado, J. M., and Serrano, D. P. (2012). Ni2P/SBA-15 as a Hydrodeoxygenation Catalyst with Enhanced Selectivity for the Conversion of Methyl Oleate into N-Octadecane. *ACS Catal.* 2 (4), 592–598. doi:10.1021/cs200659r

Yu, Z., Wang, A., Liu, S., Yao, Y., Sun, Z., Li, X., et al. (2019). Hydrodeoxygenation of Phenolic Compounds to Cycloalkanes over Supported Nickel Phosphides. *Catal. Today* 319, 48–56. doi:10.1016/j.cattod.2018.05.012

Yun, G.-N., Ahn, S.-J., Takagaki, A., Kikuchi, R., and Oyama, S. T. (2017). Hydrodeoxygenation of γ-valerolactone on Bimetallic NiMo Phosphide Catalysts. *J. Catal.* 353, 141–151. doi:10.1016/j.jcat.2017.07.006

Yusuf, N. N. A. N., Kamarudin, S. K., and Yaakub, Z. (2011). Overview on the Current Trends in Biodiesel Production. *Energy Convers. Manag.* 52 (7), 2741–2751. doi:10.1016/j.enconman.2010.12.004

Zdražil, M. (2003). MgO-supported Mo, CoMo and NiMo Sulfide Hydrotreating Catalysts. *Catal. Today* 86 (1), 151–171. doi:10.1016/S0920-5861(03)00409-7

Zhang, J., Zhao, C., Li, C., Li, S., Tsang, C.-W., and Liang, C. (2020). The Role of Oxophilic Mo Species in Pt/MgO Catalysts as Extremely Active Sites for Enhanced Hydrodeoxygenation of Dibenzofuran. *Catal. Sci. Technol.* 10 (9), 2948–2960. doi:10.1039/D0CY00341G

Zhang, Z., Tang, M., and Chen, J. (2016). Effects of P/Ni Ratio and Ni Content on Performance of γ-Al 2 O 3 -supported Nickel Phosphides for Deoxygenation of Methyl Laurate to Hydrocarbons. *Appl. Surf. Sci.* 360, 353–364. doi:10.1016/j.apsusc.2015.10.182

Zhao, C., He, J., Lemonidou, A. A., Li, X., and Lercher, J. A. (2011). Aqueous-phase Hydrodeoxygenation of Bio-Derived Phenols to Cycloalkanes. *J. Catal.* 280 (1), 8–16. doi:10.1016/j.jcat.2011.02.001

Conflict of Interest: The authors declare that the research was conducted in the absence of any commercial or financial relationships that could be construed as a potential conflict of interest.

Publisher's Note: All claims expressed in this article are solely those of the authors and do not necessarily represent those of their affiliated organizations, or those of the publisher, the editors and the reviewers. Any product that may be evaluated in this article, or claim that may be made by its manufacturer, is not guaranteed or endorsed by the publisher.